

1

2

3

4

Cosmic ray validation of electrode positions in small-strip thin gap chambers for the upgrade of the ATLAS detector

5

Lia Formenti

6

7

8

Department of Physics
McGill University, Montreal
October, 2021

9

10

11

12

13

A thesis submitted to
McGill University
in partial fulfillment of the
requirements of the degree of
Master of Science

¹⁵ Table of Contents

¹⁶	1	Introduction	1
¹⁷	2	High energy particle physics	4
¹⁸	2.1	The Standard Model	4
¹⁹	2.2	Beyond the Standard Model	6
²⁰	2.3	Studying high energy particle physics with accelerators	7
²¹	3	The LHC and the ATLAS experiment	9
²²	3.1	The Large Hadron Collider	9
²³	3.2	The High-Luminosity LHC	10
²⁴	3.3	The ATLAS experiment	12
²⁵	4	The New Small Wheels	18
²⁶	4.1	Motivation for the New Small Wheels	18
²⁷	4.2	Design of the NSWs	19
²⁸	4.3	Small-strip thin gap chambers	22
²⁹	4.4	sTGC Quadruplet Construction	25
³⁰	4.5	NSW alignment	26
³¹	5	Using cosmic muons to measure relative strip position offsets	30
³²	5.1	Cosmic rays	30
³³	5.2	Experimental setup	31

34	5.3 Data acquisition	32
35	5.4 Data preparation	32
36	5.4.1 Cuts on electrode hits	32
37	5.4.2 Clustering and tracking	33
38	5.5 Measuring relative local offsets	35
39	5.6 Visualizing relative alignment between layers	38
40	5.7 Systematic uncertainty	40
41	5.8 Discussion	42
42	6 Using x-rays to measure relative strip position offsets	43
43	6.1 Experimental setup	43
44	6.2 Data acquisition	45
45	6.3 Data preparation	45
46	6.4 Measuring local offsets	45
47	6.5 Measuring relative local offsets	47
48	7 Comparing cosmic muon and x-ray relative strip position offsets	51
49	7.1 Assessing correlation	51
50	7.2 Discussion	56
51	8 Outlook and summary	58
52	8.1 Outlook	58
53	8.2 Summary	59
54	References	60
55	APPENDICES	67
56	A Cluster position uncertainty	68
57	A.1 Cluster definition	68
58	A.2 Effect of fit algorithm on cluster mean	68
59	A.3 Effect of uncertainty in cluster mean on track residuals	69

60	B Analysis statistics	70
61	C Analysis systematics	72
62	C.1 Residual distribution fit function	72
63	C.2 Cosmic muon data collection voltage	73
64	C.3 Cluster fit algorithm	75
65	C.4 Differential non-linearity	76
66	D Printable plots	79

Abstract

68 The Large Hadron Collider (LHC) is used to generate subatomic physics processes at the
69 energy frontier to challenge our understanding of the Standard Model of particle physics.
70 The particle collision rate at the LHC will be increased up to seven times its design value in
71 2025-2027 by an extensive upgrade program. The innermost endcaps of the ATLAS muon
72 spectrometer consist of two wheels of muon detectors that must be replaced to maintain
73 the muon momentum resolution in the high-rate environment. The so-called New Small
74 Wheels (NSWs) are made of two detector technologies: micromegas and small-strip thin gap
75 chambers (sTGCs). The sTGCs are gas ionization chambers that hold a thin volume of gas
76 between two cathode boards. One board is segmented into copper readout strips of 3.2 mm
77 pitch that are used to precisely reconstruct the coordinate of a passing muon. Modules of
78 four sTGCs glued together into quadruplets cover the NSWs. Quadruplets were designed
79 to achieve a 1 mrad angular resolution to fulfill the spectrometer's triggering and precision
80 tracking requirements. To achieve the required angular resolution the absolute position of
81 the readout strips must be known in the ATLAS coordinate system to within 100 μm . At
82 McGill University, the performance of sTGC quadruplets was characterized using cosmic ray
83 data before being sent to CERN, where the charge profile left by x-rays is used to measure
84 the offset of the strip patterns with respect to nominal at a limited number of points on
85 the surface of each quadruplet. The x-ray strip position measurements have acceptable but
86 limited precision and do not span the whole area of the strip layers. Given the importance of
87 knowing the absolute position of each readout strip to achieve the performance requirements
88 of the NSWs, the x-ray method must be validated by an independent method. Cosmic ray
89 data is used to characterize the relative alignment between layers and validate the x-ray
90 method.

Résumé

Le collisioneur LHC est utilisé pour générer des processus de la physique subatomique à la frontière d'énergie pour remettre en cause le modèle standard de la physique des particules. Le taux des collisions du collisioneur LHC augmentera jusqu'à sept fois le taux nominal en 2025-2027 par un programme d'amélioration majeur et varié. Une partie du spectromètre à muons est composée de deux roues de détecteurs de muons qu'il faut remplacer pour maintenir la résolution d'élan après l'augmentation du taux. Appelées les Nouvelles Petites Roues (NSWs), elles en utilisent deux technologies: des chambres micromegas et des chambres sTGCs (chambres à petites bandes et à intervalles fins). Les sTGCs sont des chambres d'ionisation de gaz, qui contiennent un volume de gaz fin entre deux panneaux cathodiques. Un panneau est segmenté à petites bandes en cuivre avec une pente de 3.2 mm qui se servent comme des voies de signal pour reconstruire précisément la coordonnée d'un muon qui passe. Des modules de quatre sTGCs collés ensemble en quadruplets couvrent les NSWs. Les quadruplets étaient conçus pour réaliser une résolution angulaire de 1 mrad pour satisfaire les exigences des systèmes de déclenchement et de mesures de précision. Pour réaliser la résolution angulaire il faut que la position absolue de chaque bande soit connue dans ATLAS avec une précision à moins de 100 μm . À l'Université de McGill, la performance des quadruplets étaient caractériser avec des rayons cosmiques avant les envoyer à CERN, où le profil de charge laisser par des rayons-X est utilisé pour mesurer le déplacement du motif des bandes par rapport à nominal à un nombre de position limité sur la surface des quadruplets. Les déplacements mesurés pas les rayons-X ont une précision acceptable mais limitée, et ne couvrent pas la région entière des panneaux. Étant donné l'importance de savoir la position absolue de chaque bande pour réaliser les exigences de performance des NSWs, il faut une méthode indépendante pour valider la méthode des rayons-X. Les données recueillies avec les rayons cosmiques sont utilisées pour charactariser l'alignement relatif entre les panneaux et pour valider la méthode des rayons-X.

Acknowledgements

- 118 Experimental particle physics projects are never done alone. I am grateful to have been
119 working with the ATLAS Collaboration for two years now.
- 120 Thank you to Dr. Brigitte Vachon for her guidance throughout this project and for editing
121 this thesis. I am consistently amazed by her ability to jump into the details of my project
122 and discuss them with me.
- 123 Thanks also to Dr. Benoit Lefebvre, who collected some of the data used in this thesis, wrote
124 several software tools I used to analyze the data and advised me several times throughout
125 this project.
- 126 Thank you to my labmates at McGill University, Dr. Tony Kwan, Kathrin Brunner, John
127 McGowan and Charlie Chen. Kathrin taught me mechanical skills that I will apply elsewhere.
128 Tony, manager of the laboratory, created the most encouraging, trusting and productive work
129 environment I have ever been apart of.
- 130 Thank you to the friends I can call on at anytime, and thank you to my family whose
131 constant support makes every step possible.

Contribution of authors

I, the author, was involved in collecting the cosmic ray data from September 2019 - March 2021. I did not design the cosmic ray testing procedure nor write the data preparation software, but I participated in using the software to analyze cosmic ray results. In the thesis, the terms “clustering,” “local offset” and “relative local offset” are defined. Cosmic ray clustering was done in the data preparation software, but I redid the fit afterwards to explore sensitivity to the fit algorithm. With help from Dr. Lefebvre and Dr. Vachon, I helped design the software that calculated the relative local offsets from cosmic ray data. I wrote that software on my own. I was not involved in the design, data collection, data preparation or analysis of the x-ray data. I also was not involved in creating an alignment model from the x-ray data. I used the x-ray local offsets calculated using x-ray data analysis software to calculate relative local offsets with x-rays. I did the comparison between the x-ray and cosmic ray data.

I hereby declare that I am the sole author of this thesis. This is a true copy of the thesis, including any required final revisions, as accepted by my examiners.

¹⁴⁷

Chapter 1

¹⁴⁸

Introduction

¹⁴⁹ The Standard Model (SM) is a theoretical framework that describes experimental observa-
¹⁵⁰ tions of particles and their interactions at the smallest distance scales; however, the questions
¹⁵¹ the SM does not address motivate more experimentation.

¹⁵² Accelerators collide particles to generate interactions that can be recorded by detectors
¹⁵³ for further study. Detectors measure the trajectory and energy of all secondary particles
¹⁵⁴ produced in collisions to understand the interaction. The Large Hadron Collider (LHC) [1]
¹⁵⁵ at CERN is the world’s most energetic particle accelerator. Its energy makes it a unique
¹⁵⁶ tool to study elementary particles and their interactions in an environment with conditions
¹⁵⁷ similar to what would have existed in the early universe. If study at the energy frontier is
¹⁵⁸ to continue, the LHC must go on.

¹⁵⁹ After 2025, the statistical gain in running the LHC further without significant increase in
¹⁶⁰ beam intensity will become marginal. The High Luminosity Large Hadron Collider (HL-
¹⁶¹ LHC) project [2] is a series of upgrades to LHC infrastructure that will allow the LHC
¹⁶² to collect approximately ten times more data than in the initial design by \sim 2030. The
¹⁶³ increase in LHC beam intensity will result in a large increase in collision rate that will make
¹⁶⁴ accessible and improve statistics on several measurements of interest [3], many only possible
¹⁶⁵ at the LHC and the energy frontier. The increase in beam intensity will also increase the
¹⁶⁶ level of background radiation, requiring major upgrades to the experiments used to record
¹⁶⁷ the outcomes of the particle collisions.

¹⁶⁸ The ATLAS experiment [4] is one of the LHC’s general-purpose particle detector arrays, po-
¹⁶⁹ sitioned around one of the collision points of the LHC. During the 2019-2022 Long Shutdown
¹⁷⁰ of the LHC, the most complex upgrade of the ATLAS experiment is the replacement of the
¹⁷¹ small wheels of the muon spectrometer with the so-called New Small Wheels (NSWs) [5].

172 The detector upgrade addresses both the expected decrease in hit efficiency of the precision
173 tracking detectors and the high fake trigger rate expected in the muon spectrometer at the
174 HL-LHC. The NSWs are made of two different detector technologies: micromegas and small-
175 strip thin gap chambers (sTGCs). Micromegas are optimized for precision tracking while
176 sTGCs are optimized for rapid triggering, although each will provide complete coverage and
177 measurement redundancy over the area of the NSWs. Eight layers each of sTGCs cover the
178 NSWs. Practically, countries involved in detector constructor created quadruplet modules of
179 four sTGCs glued together that were arranged and installed over the area of the NSWs once
180 they arrived at CERN. Teams across three Canadian institutions built and characterized 1/4
181 of all the required sTGCs.

182 The sTGCs are gas ionization chambers that consist of a thin volume of gas held between two
183 cathode boards. One board is segmented into strip readout electrodes of 3.2 mm pitch. The
184 position of the particle track in the precision coordinate can be reconstructed from the strip
185 signals [5]. The sTGCs achieved the design track spatial resolution in the precision coordinate
186 of less than 100 μm per detector plane that will allow them to achieve a 1 mrad track angular
187 resolution using the 8 layers of sTGC on the NSW [6, 5]. The NSW measurement of the
188 muon track angle will be provided to the ATLAS trigger and used to reject tracks that do
189 not originate from the interaction point [5].

190 The precise measurement of a muon track angle depends on knowing the position of each
191 readout strip within the ATLAS coordinate system. To achieve this, the position of specific
192 locations on the surface of sTGC quadruplets will be monitored by the ATLAS alignment
193 system to account for time-dependent deformations [5]. Within a quadruplet module, the
194 strip positions could have been shifted off of nominal by non-conformities of the strip pattern
195 etched onto each cathode boards [7] and shifts between strip layers while gluing sTGCs into
196 quadruplets.

197 An xray gun was used to measure the offset of strips from their nominal position at the
198 locations that will be monitored by the ATLAS alignment system thereby providing, locally,
199 an absolute “as-built” strip position within the ATLAS coordinate system. Estimates of the
200 “as-built” positions of every readout strip are obtained by building an alignment model from
201 the available x-ray measurements [8].

202 The technique of measuring the “as-built” strip positions using xray data has never been
203 used before and must be validated. This thesis describes the use of cosmic muon data,
204 recorded to characterize the performance of each Canadian-made sTGC module, to validate
205 the x-ray strip position measurements. A description of how this work fits within the overall
206 alignment scheme of the NSW is also presented.

207 *Rewrite after implementing Brigitte’s edits.* Chapters 3 and 4 give more background on
208 particle physics, the LHC, ATLAS, the NSWs, and sTGCs. In chapter 5, the cosmic ray

209 testing procedure and how the position of the strips can be probed with cosmics data is
210 presented. Chapter 6 introduces the x-ray method, and in chapter 7, the x-ray offsets are
211 validated with cosmic muon data. The thesis concludes with a summary and outlook in
212 chapter 8.

²¹³ Chapter 2

²¹⁴ High energy particle physics

²¹⁵ Particle physics aims to study the elementary constituents of matter. Understanding the fundamental building blocks and how they interact provides insight into how the early universe evolved to the forms of matter we observe today. This chapter introduces general concepts in particle physics relevant to understanding the physics goals of the High-Luminosity LHC (HL-LHC) and NSWs upgrade.

²²⁰ The information on particle physics and the SM presented here is rather general; the interested reader is referred to [9, 10, 11] for more information.

²²² 2.1 The Standard Model

²²³ The Standard Model (SM) is a theoretical framework developed in the early 1970's that describes the observed elementary particles and their interactions. It is built on a collection of quantum field theories and has been remarkably successful at predicting experimental observations, including but not limited to the existence of the top quark [12], the tau neutrino [13] and the Higgs boson [14, 15].

²²⁸ The known elementary particles described by the SM are represented in figure 2.1. There are 12 matter particles (six quarks and six leptons), 4 force-mediating particles, and the Higgs boson. Each matter particle also has an anti-matter particle pair with the same mass but opposite charge, not represented in figure 2.1. The different forces of nature are understood to be the result of the exchange of force-mediating particles between interacting (coupled) particles. Photons are mediators of the electromagnetic force, W⁺/- and Z bosons are mediators of the weak force, and gluons are mediators of the strong force. At high

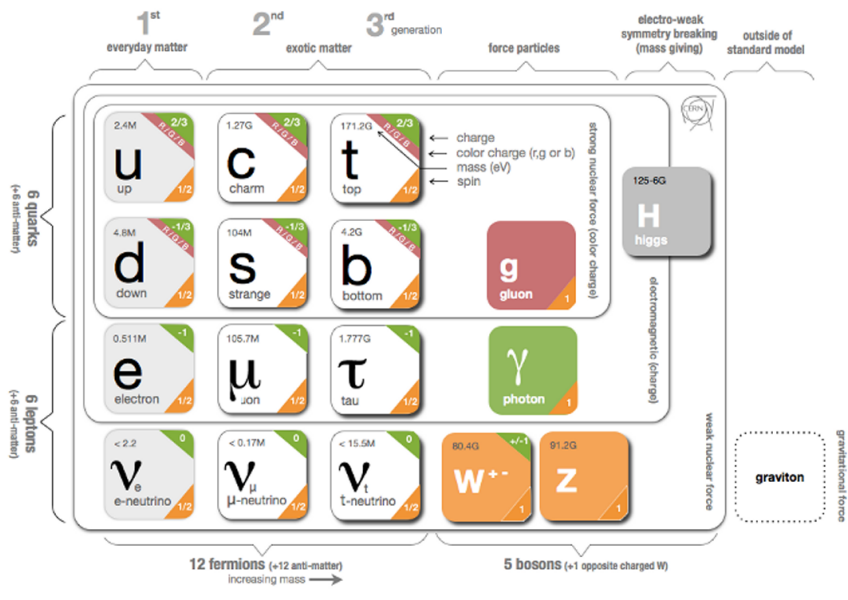


Figure 2.1: Schematic diagram of all elementary particles in the SM. Particles are grouped according to their properties and the forces through which they interact with other particles [16].

235 energy, the SM describes the electromagnetic and weak forces as stemming from a unified
236 electroweak force. The Higgs boson field interacts with the particles mediating the unified
237 electroweak force to distinguish the weak and electromagnetic forces from each other at lower
238 energies and give particles (except neutrinos) a mass. This is called electroweak symmetry
239 breaking.

240 Quarks are matter particles that are sensitive to all forces; notably they are the only particles
241 sensitive to the strong force. Protons and neutrons are made up of quarks and gluons, and the
242 strong force is responsible for their existence and mutual attraction into nuclei [17]. Leptons
243 are particles not sensitive to the strong force. Charged leptons include the electron, which
244 once part of atoms is responsible for chemistry. Of particular importance for this thesis is
245 the charged lepton called a muon. It is like the electron but its mass is \sim 200 times larger
246 than that of the electron. Muons have a lifetime of $2.2\ \mu\text{s}$ [11] and decay predominantly as
247 $\mu \rightarrow e^-\bar{\nu}_e\nu_\mu$. Neutrinos are neutral, almost massless leptons that only interact through the
248 weak force.

249 Common matter is made up of the lightest constituents of the SM: up and down quarks,
250 electrons and photons. The other particles are produced in high-energy environments but
251 then decay to the lightest constituents. Such high energy environments include the condi-
252 tions present in the early universe [18], astrophysical sources, and particle accelerators. The
253 presence of the particles of the SM at the beginning of the Universe means that their inter-
254 actions and decays are fundamental for the study of the evolution of the early universe [18].
255 Many high energy astrophysical sources, like supernovae, generate particles that rain down
256 on Earth as cosmic rays [19]. Particle accelerators have been built to create controlled en-
257 vironments of high-rate, high-energy particle collisions at high energy where the production
258 and decay of elementary particles can be directly studied.

259 2.2 Beyond the Standard Model

260 Despite its success at describing most experimental observations to date, there is ample
261 evidence that the SM is not a complete description of natural phenomena at the smallest
262 scales. For example, the SM has a large number of free parameters, the values of which have
263 to be fine-tuned to fit experimental observations. This is part of the so-called “naturalness”
264 problem.

265 Furthermore, the SM provides no explanation for several open questions in particle physics.
266 First, neutrinos in the SM are assumed to be massless and do not gain mass in the same way
267 as the other particles. However, neutrino were confirmed to change between their different
268 flavours in 2013 [20], which can only occur if neutrinos do have mass [21]. The neutrino

269 mass requires physics beyond the standard model [22]. Second, several astrophysical and
270 cosmological measurements suggest the presence of “dark matter” making up 85 % of the
271 matter content of the universe [23]. The nature of dark matter is unknown and so far there
272 is no SM explanation [24]. Third, the SM does not explain the origin and nature of the
273 matter-antimatter asymmetry that produced our matter-dominated universe. Finally, the
274 SM does not include a description of gravity.

275 Theoretical extensions beyond the Standard Model (BSM) aim to address some of these
276 questions, often predicting existence of yet-unseen elementary particles or physics phenomena
277 beyond those predicted by the SM. These hypothetical new physics phenomena or new
278 particles can be searched for at particle accelerators.

279 **2.3 Studying high energy particle physics with accelerators**

280

281 In particular, particle accelerators of increasingly higher energy have a long history of en-
282 abling the discovery of predicted particles. These include, for example, the discovery of
283 the W [25, 26] and Z bosons [27, 28], the top quark [29, 30], and most recently, the Higgs
284 boson [31, 32]. The discovery of the Higgs boson marked the completion of the SM as it is
285 known today.

286 Based on the established success of the SM, there are two approaches to particle physics
287 research. One approach is to search for the existence of new physics phenomena predicted
288 to exist in BSM theories and the other is to test the validity of the SM to a high degree of
289 accuracy to search for flaws in the model. Standard Model predictions are generally expressed
290 in terms of the probability of a specific physics process to occur, expressed as a cross section
291 in units of barns (with 1 barn = 10^{-28} m²). As an example, figure 2.1 shows a summary
292 of cross section measured for different physics processes using the ATLAS experiment and
293 their comparison with the predictions of the SM. Most cross section measurements agree
294 well within one standard deviation with the SM predictions.

295 Particle accelerators provide a controlled and high-collision rate environment that makes
296 them ideal places to search for new physics phenomena and to carry out systematic tests of
297 the SM. The LHC is the highest energy collider in the world so it can access physics that
298 no other accelerator can. A description of the LHC and the ATLAS detector are provided
299 in the next chapter.

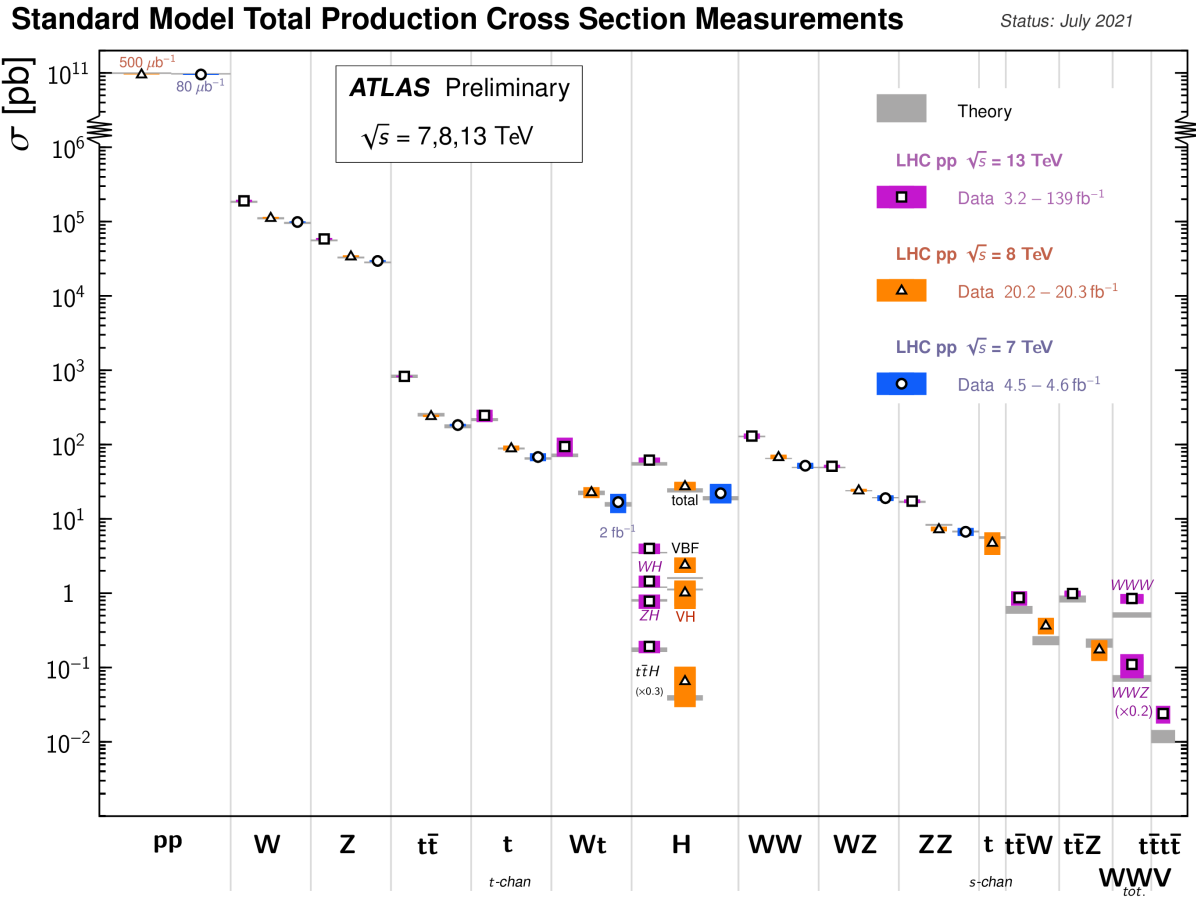


Figure 2.2: Production cross sections of different final states measured by the ATLAS experiment at the LHC. Comparison with the SM theory predictions is also shown [33].

300 **Chapter 3**

301 **The LHC and the ATLAS experiment**

302 The Large Hadron Collider (LHC) is the world’s most energetic particle accelerator and the
303 ATLAS experiment is used to record the results of particle collisions at the LHC. In this
304 chapter, details about both that are necessary to understand the High-Luminosity LHC (HL-
305 LHC) upgrade project and the ATLAS experiment’s New Small Wheels (NSWs) upgrade
306 are presented.

307 **3.1 The Large Hadron Collider**

308 The LHC is an accelerator 27 km in circumference and located \sim 100 m underground at
309 the CERN laboratory near Geneva, Switzerland [1]. It has two beam pipes within which
310 bunches of protons counter-circulate before being collided in the center of one of four major
311 experiments, such as the ATLAS experiment (discussed in section 3.3). Protons are guided on
312 the circular trajectory using 1232 superconducting dipole magnets capable of a maximum
313 field of 8.33 T. Radio-frequency accelerating cavities are used to accelerate protons to a
314 the maximum design energy of 7 TeV [34]. During LHC Run-1 (2011-2012), protons were
315 collided at a collision center-of-mass energy of 7 TeV and 8 TeV [35]. During LHC Run-2
316 (2015-2018), the center-of-mass energy of proton collisions was increased to 13 TeV [36],
317 close to the maximum design value of 14 TeV [34]. It is not actually the protons that
318 interact, but the constituent quarks and gluons that each carry some fraction of the energy
319 and momentum of the collisions.

320 **Luminosity**

321 The number of proton-proton interactions generated by the LHC directly affects the statistics

available to make measurements of interaction cross sections. Predicting the number of proton-proton interactions requires defining a metric called luminosity [11]. The luminosity of a particle collider is the number of particles an accelerator can send through a given area per unit time. It is calculated from the measurable quantities in Equation 3.1:

$$\mathcal{L} = \frac{f N_1 N_2}{4\pi\sigma_x\sigma_y}, \quad (3.1)$$

where f is the frequency of the bunch crossings (25 ns), N_1 and N_2 are the number of protons in each bunch ($\sim 10^{11}$ protons / bunch), and σ_x and σ_y are the RMS of the spatial distributions of the bunch. Therefore, luminosity is a property of accelerator beams, which are set by the capabilities of the accelerator. The design luminosity of the LHC was $10^{34} \text{ cm}^{-2}\text{s}^{-1}$. The units of luminosity are an inverse area; multiplying the luminosity by the cross section of a given process gives the expected rate for that process.

Integrating the *instantaneous* luminosity (equation 3.1) over a period of data collection time gives the integrated luminosity,

$$L = \int \mathcal{L}(t) dt \quad (3.2)$$

which is related to the total number of interactions. In this way, the luminosity is the link between the accelerator and the statistical power of measurements to be made with the data collected. So far, the LHC provided an integrated luminosity of 28.26 fb^{-1} in Run-1 [35] and 156 fb^{-1} in Run-2 [36].

3.2 The High-Luminosity LHC

At the end of the LHC program in 2025, the statistical gain on measurements in running the LHC further will become marginal. The HL-LHC [2] project consists of the upgrade of LHC infrastructure to achieve a nearly ten fold increase in instantaneous luminosity, thereby improving measurement statistics as well. Also, some systems will need repair and replacement to operate past ~ 2020 . The LHC will continue to be the most energetic accelerator in the world for years to come and is the only accelerator with enough energy to directly produce the Higgs boson and top quarks. Therefore, the European Strategy for Particle Physics made it a priority “to fully exploit the physics potential of the LHC” with “a major luminosity upgrade” [37]. The goal is for the HL-LHC to provide an integrated luminosity of 3000 fb^{-1} in the 12 years following the upgrade. The luminosity actually



Figure 3.1: The LHC/HL-LHC timeline [38]. The integrated luminosities collected and projected for each run of the LHC are shown in blue boxes below the timeline and the center of mass energy of the collisions is shown in red above the timeline. The top blue arrow labels the run number. The acronym “LS” stands for “long shutdown” and indicates periods where the accelerator is not operating. During the shutdowns, upgrades to the LHC and the experiments are taking place. This timeline was last updated in January, 2021, and reflects changes in the schedule due to the ongoing pandemic.

349 achieved will depend on a combination of technological advances and upgrades in progress
 350 that affect the factors contributing to luminosity defined in equation 3.1 [2]. Figure 3.1 shows
 351 the projected schedule of the HL-LHC upgrades and operation [38].

352 One of the most anticipated measurements at the HL-LHC is the value of the triple-Higgs
 353 coupling. Measuring the coupling will allow the determination of the shape of the Higgs
 354 potential responsible for electroweak symmetry breaking. Any discrepancy with respect to
 355 the SM prediction will show that there must be other sources of electroweak symmetry
 356 breaking, and hence physics phenomena beyond the SM. The LHC is the only accelerator
 357 where the Higgs boson can be produced directly so it is the only place where the triple-Higgs
 358 coupling could be measured. The HL-LHC upgrade is required to produce a significant
 359 sample of Higgs produced in pairs to make a statistically meaningful measurement [3, 39].

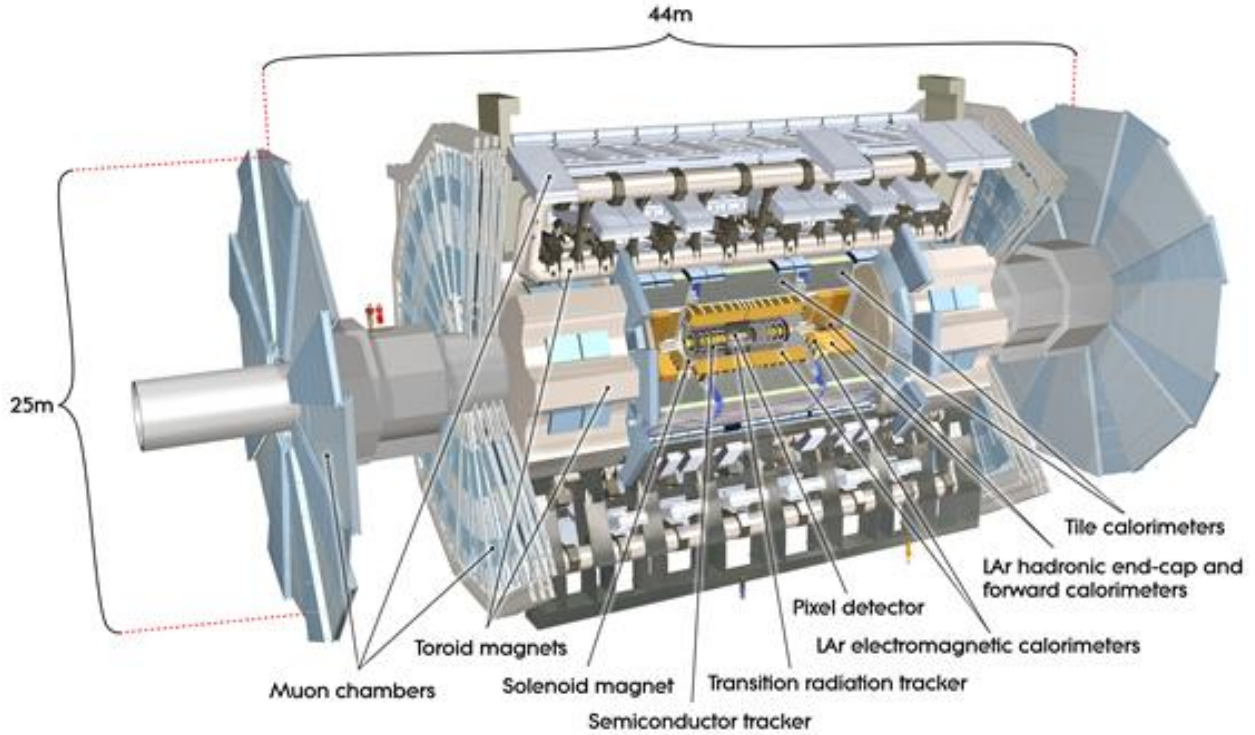


Figure 3.2: Schematic diagram of the ATLAS experiment, with the various detector subsystems labelled [4].

360 Accordingly, detector sensitivity to various Higgs decays will be important at the HL-LHC.

361 3.3 The ATLAS experiment

362 The ATLAS experiment [4] was designed to support all the physics goals of the LHC. It
363 is 44 m long and 25 m in diameter, and weighs 7000 tonnes. The ATLAS experiment is
364 centered around one of the LHC's interaction points (a place where the beams collide). As
365 shown schematically in figure 3.2, ATLAS consists of an array of particle detector subsystems
366 arranged concentrically around the beam pipe. The ATLAS experiment is cylindrical because
367 it aims to provide 4π coverage around the interaction point. In reference to the cylindrical
368 geometry of the experiment, it is helpful to separate the subsystems of ATLAS into the
369 so-called "barrel" and "endcap"/"forward" regions.

370 For analysis purposes, a spherical coordinate system is defined. The azimuthal angle ϕ is
371 measured around the beampipe and the polar angle θ is measured from the beam pipe. The
372 polar angle is more often expressed in terms of pseudo-rapidity, defined as $\eta = -\ln \tan(\theta/2)$.
373 Pseudo-rapidity values vary from 0 (perpendicular to the beam) to $\pm\infty$ (parallel to the
374 beam, defined as the z-direction) and is an approximation to the rapidity of a particle when
375 its momentum is much greater than its mass. It is useful to describe the direction of outgoing
376 particles in proton-proton collisions because differences in rapidity are invariant to a Lorentz
377 boost along the beam direction.
378 The ATLAS experiment provides identification and kinematic measurements for each particle
379 created after the initial collision, which is done by assembling offline the information recorded
380 by each subsystem. With this information, signatures of processes of interest can be identified
381 and studied. An overview of the main ATLAS subsystems is given below.

382 **The inner detector**

383 The inner detector [40, 41] (figure 3.3) is for precise measurements of charged particle tra-
384 jectories, measurement of primary and secondary interaction vertices and assistance in the
385 identification of electrons. A 2 T solenoid with field parallel to the beam bends the trajec-
386 tory of outgoing charged particles. A measurement of the bending radius of each charged
387 particle provides information about its momentum. The innermost part of the inner tracker
388 is made of high-resolution semiconductor pixel and strip detectors while the outermost part
389 is made of straw-tubes. The straw tubes are used in the trajectory measurements but they
390 are also interspersed with material designed to enhance the creation of transition radiation.
391 Transition radiation occurs when a highly relativistic charged particle traverses a material
392 boundary [42]. The amount of transition radiation emitted by a charged particle is detected
393 by the straw-tubes and is used to identify electrons.

394 **Calorimetry system**

395 Electromagnetic and hadronic sampling calorimeter units are used to record the energy
396 of electrons, photons and jets¹. A combination of liquid-argon (LAr) electromagnetic and
397 hadronic calorimeters [43] and tile-scintillator hadronic calorimeters [44] cover the rapidity
398 range $|\eta| < 4.9$, as shown in figure 3.4.
399 Sampling calorimeters have alternating layers of dense material and material that can mea-
400 sure the amount of ionization by charged particles. The dense material causes incoming

¹When quarks or gluons are expelled in a high energy collision, they create collimated groups of hadrons because they carry a charge called “colour”, and nature only allows “colourless” combinations to exist [42].

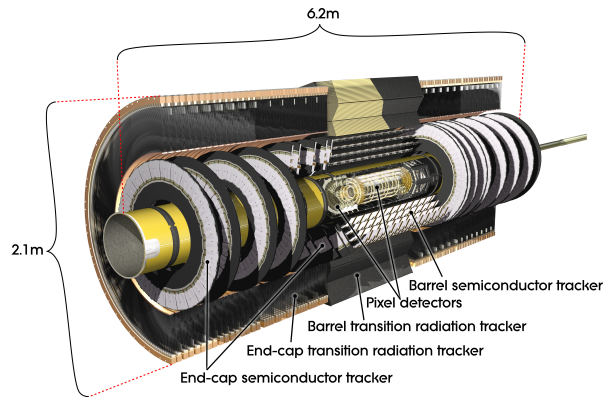


Figure 3.3: Schematic diagram of the ATLAS experiment's inner detector, with the different segments and the technology used labeled [4].

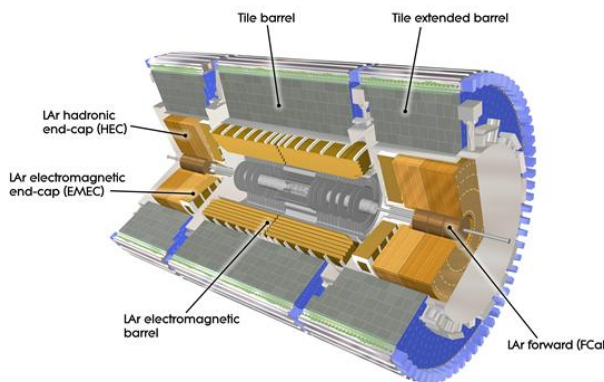


Figure 3.4: Schematic diagram of the ATLAS calorimeter system, with the different segments and the technology used labeled [4].

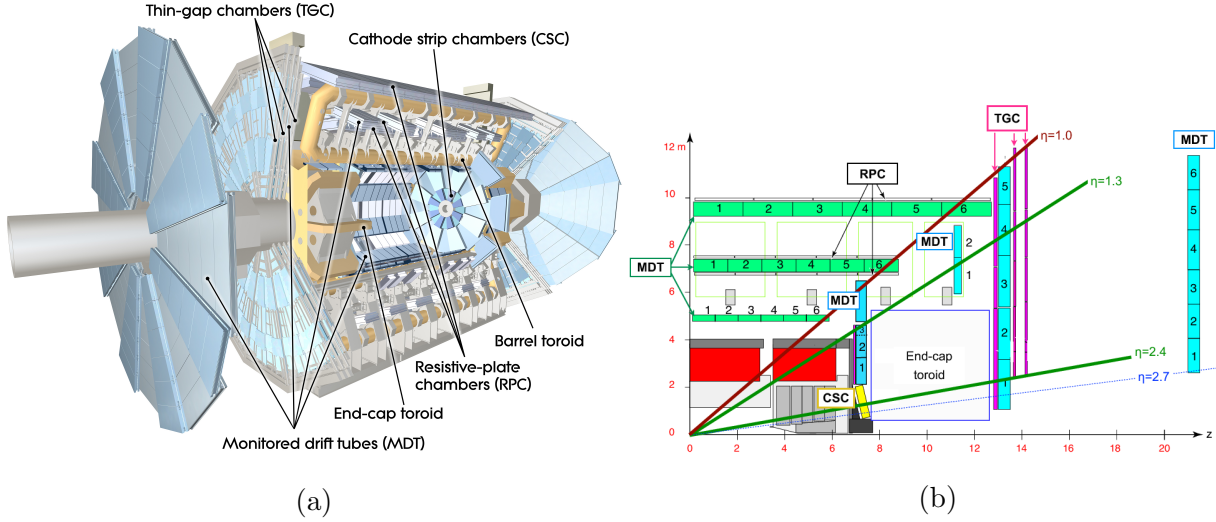


Figure 3.5: Schematic diagram of the ATLAS muon spectrometer. Figure (a) shows a 3D projection of the system with the different types of chambers and different parts of the toroidal magnet system labeled [4]. Figure (b) shows a projection of one quarter of the muon spectrometer, with the interaction point in the bottom left corner. The small wheel is just left of the end cap toroid, the big wheel is to its right, and the outer wheel is the rightmost structure [47].

401 charged particles to shower into lower energy particles and deposit their energy in the sen-
 402 sitive volume. Only muons and neutrinos are known to pass the calorimeters to the muon
 403 spectrometer without being absorbed.

404 Muon spectrometer

405 The muon spectrometer [45] consists of multiple layers of tracking chambers embedded in
 406 a 2 T magnetic field generated by an air-core superconducting toroid magnet system. Fig-
 407 ure 3.5a shows a schematic diagram of the layout of the different chambers and of the toroid
 408 magnets [4]. The trajectory of a muon is reconstructed from the information recorded by
 409 the different types and layers of tracking chambers. The amount of bending in the magnetic
 410 field provides a measure of the muon's momentum. In the barrel section of ATLAS, the
 411 toroidal magnetic field is created by eight coils bent into the shape of a "race-track" and
 412 symmetrically arranged around the beampipe. In the forward region, two end-cap toroids,
 413 each with eight smaller racetrack-shaped coils arranged symmetrically around the beam pipe
 414 are inserted in the ends of the barrel toroid [46].

415 The muon spectrometer is separated into detectors used for precision offline tracking and

416 for triggering purposes. Three layers of monitored drift tubes (MDTs) or cathode strip
417 chambers (CSCs) are used for tracking. The position of the muon track in each of the three
418 layers allows reconstruction of the bent trajectory of a muon and hence its momentum. To
419 satisfy the muon spectrometer target momentum resolution of $\Delta p_T/p_T < 1 \times 10^{-4}$ p / GeV
420 for $p_T < 300$ GeV and a few percent for lower p_T muons, the MDTs and CSCs were designed
421 to achieve a spatial resolution of 50 μm each. Accordingly, an optical alignment system was
422 designed to monitor and correct for chamber positions [45, 48].

423 Resistive plate chambers (RPCs) are used for triggering in the barrel and thin-gap chambers
424 (TGCs) are used for triggering in the endcaps. The positions of each type of chamber
425 are sketched in figure 3.5b. The endcap section of the muon spectrometer consists of three
426 sections, the small wheel, big wheel, and outer wheel – ordered by proximity to the interaction
427 point. In Run-1, low (high) p_T muons were triggered on if two (three) of the RPC or TGC
428 layers around the big wheel fired in coincidence, for the barrel and endcaps respectively [49].
429 After Run-1 it was discovered that up to 90% of the triggers in the endcap were fake, caused
430 by background particles generated in the material between the small wheel and the big
431 wheel [5]. To reduce the fake rate in Run-2, the TGCs on the inside of the small wheel also
432 had to register a hit. The added condition reduced the trigger rate by 50% in the range $1.3 < |\eta| < 1.9$ [50]. The effectiveness of the solution was limited since the $|\eta|$ -range of the small
434 wheel TGCs was limited to $1.0 < |\eta| < 1.9$ and the spatial resolution of the small wheel
435 TGCs is coarse [5].

436 Trigger system

437 It would be impossible to record all the data from bunch crossings every 25 ns, corresponding
438 to a rate of ~ 40 MHz. The ATLAS experiment has a multi-level trigger system to select
439 events of interest for permanent storage. The Level-1 (L1) hardware trigger [49] uses partial-
440 granularity information from the muon spectrometer and calorimeters to trigger on high p_T
441 muons, electrons, jets, missing transverse energy, and τ decaying to hadrons. After Run-3
442 an upgrade of the trigger system will allow a maximum trigger rate of 1 MHz with a latency
443 of 10 μs [51], but for now the working limits are a rate of 100 kHz [50] and 2.5 μs [49].

444 The L1 trigger is used to define regions of interest that are fed into the software high level
445 trigger (HLT) [52], in which the full granularity of the muon spectrometer and calorimeter
446 are used with information from the inner detector to reduce the trigger rate to 1 kHz. Events
447 that satisfy at least one of the L1 and HLT trigger criteria are recorded to permanent storage
448 for offline analysis.

450 With the foreseen increase in luminosity at HL-LHC, it is a priority to upgrade the ATLAS
451 detector to further reduce the muon trigger fake rate in the forward region. The New Small
452 Wheels being commissioned to replace the original ATLAS muon small wheels will address
453 this challenge.

454 **Chapter 4**

455 **The New Small Wheels**

456 **4.1 Motivation for the New Small Wheels**

457 The hit rate of all detector systems will significantly increase during HL-LHC operation
458 because of the increase in luminosity. The increased rate presents a challenge for both the
459 tracking and triggering capabilities of the muon spectrometer [5].

460 In terms of precision tracking, the maximum hit rate in the MDTs is expected to reach above
461 300 kHz by the end LHC operation. At this rate, the hit efficiency of MDTs decreases by
462 35%, mostly due to the long dead-time of the chambers. Losing hits in the small wheel will
463 reduce the high p_T muon momentum resolution. The decrease in resolution will affect the
464 ability to search for, for example, the decay of hypothetical heavy bosons (W' , Z') or other
465 hypothetical particles beyond the SM [3].

466 Already during LHC Run-2 operation, the forward muon trigger system had to cope with a
467 very high fake rate, even with the inclusion of TGC data from the small wheel as part of the
468 trigger criteria. At the luminosity expected in Run-3, it is estimated that 60 kHz out of the
469 maximum L1 trigger bandwidth of 100 kHz would be taken up by forward muon triggers.
470 To address this challenge, a possible solution would be to raise the minimum p_T threshold
471 from 20 GeV to 40 GeV. However, this would have an adverse impact on the ability to study
472 several physics processes of interest that depend on low p_T muons, particularly the Higgs
473 decay to two muons, the Higgs decay to two tau leptons and hypothetical particle decays
474 beyond the SM [5].

475 The NSWs will address both of these problems. They will be made of precision tracking
476 chambers suitable for the expected hit rates during the HL-LHC and triggering chambers
477 capable of 1 mrad track angular resolution. The idea behind the design triggering capability

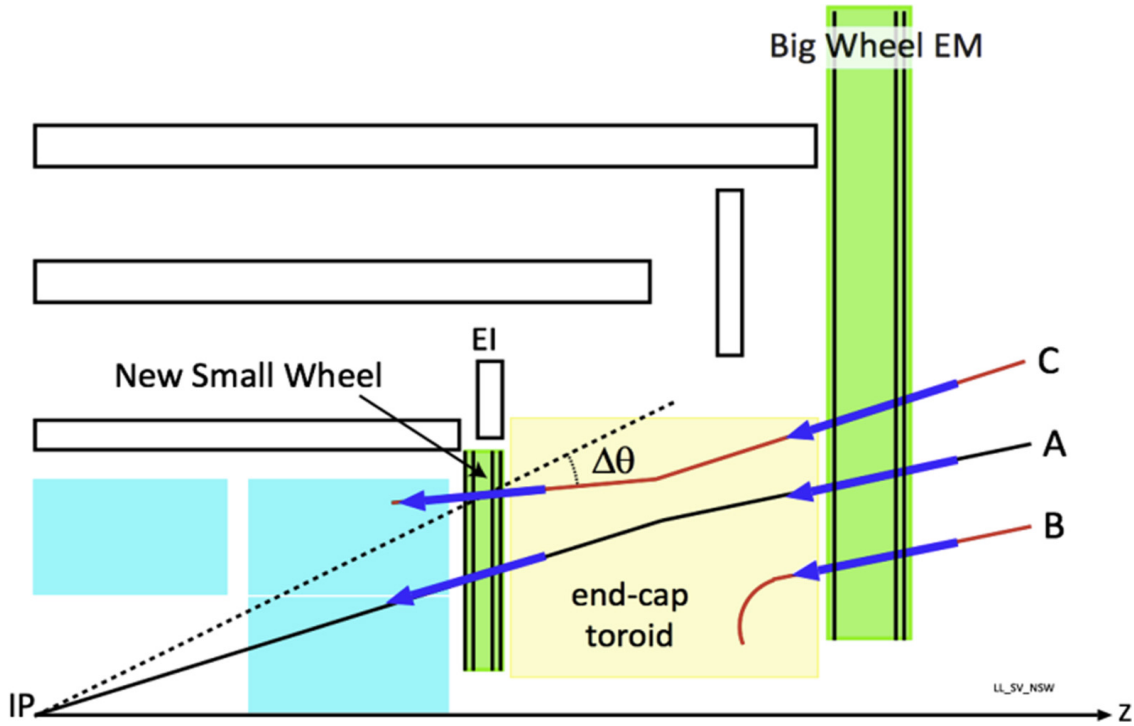


Figure 4.1: A schematic diagram of a quarter cross section of the ATLAS muon spectrometer, with the interaction point (IP) in the bottom left corner. Three possible tracks are labeled. Ideally, track A would be triggered on while track B and C discarded. With the old small wheel, all three tracks would be recorded. With the NSW, only track A would be recorded [5].

478 of the chambers is to allow matching of track segments measured by the NSW with track
 479 segments from the big wheel to discard tracks not originating from the interaction point.
 480 Figure 4.1 illustrates this point: the Run-2 trigger system would have triggered on all three
 481 tracks (A, B, C) while with the NSW the trigger system would only trigger on track A.
 482 The NSWs will therefore make it possible to maintain a low muon p_T trigger threshold and
 483 maintain an adequate muon momentum resolution during HL-LHC operations, which will
 484 allow the full exploitation of the physics potential of this research program [5].

485 4.2 Design of the NSWs

486 The NSWs are made with two detector technologies: micromegas and small-strip thin gap
 487 chambers. Eight layers of each cover the entire area of the wheel. Micromegas are designed

488 to be the primary precision tracking detectors and sTGCs the primary triggering detectors,
489 but both technologies offer full redundancy by being capable of providing both precision
490 measurements and trigger information. Both types of detectors were designed to achieve
491 spatial resolution better than $\sim 100 \mu\text{m}$ per layer. Four chambers are glued together to create
492 quadruplet modules of each detector type. Quadruplets of different sizes, most shaped as
493 trapezoids, are assembled into wedges. Two sTGC wedges and two micromegas wedges are
494 layered to create sectors (with the sTGC wedges on the outside) [5]. Different stages of the
495 construction process are shown in figure 4.2. At the time of writing, the assembly of the
496 NSWs has just been completed. The first NSW has been lowered into the ATLAS cavern
497 and is being commissioned and the second will be lowered shortly.



(a) A sTGC quadruplet module. The left image highlights the trapezoidal shape of a quadruplet module. The right image shows the corner at the short edge, where the four sTGC layers and each layer's gas inlet are visible. The gas outlets and high voltage cables are located along the long edge near the corner in the back left of the photo. The green printed circuit board along the sides are the adaptor boards where the front end electronics are attached.



(b) Left: A sTGC wedge. The white frame outlines the individual quadruplet modules that have been glued together into a wedge. Right: A completed sector, with two sTGC wedges on the outside and two micromegas wedges on the inside.



(c) A picture of one of the two NSWs. All sectors except one large sector at the top are installed, revealing two of the smaller sectors that are normally hidden under the large sectors and support bars. The NSWs are 9.3 m in diameter.

Figure 4.2: Images showing different stages of NSW construction.

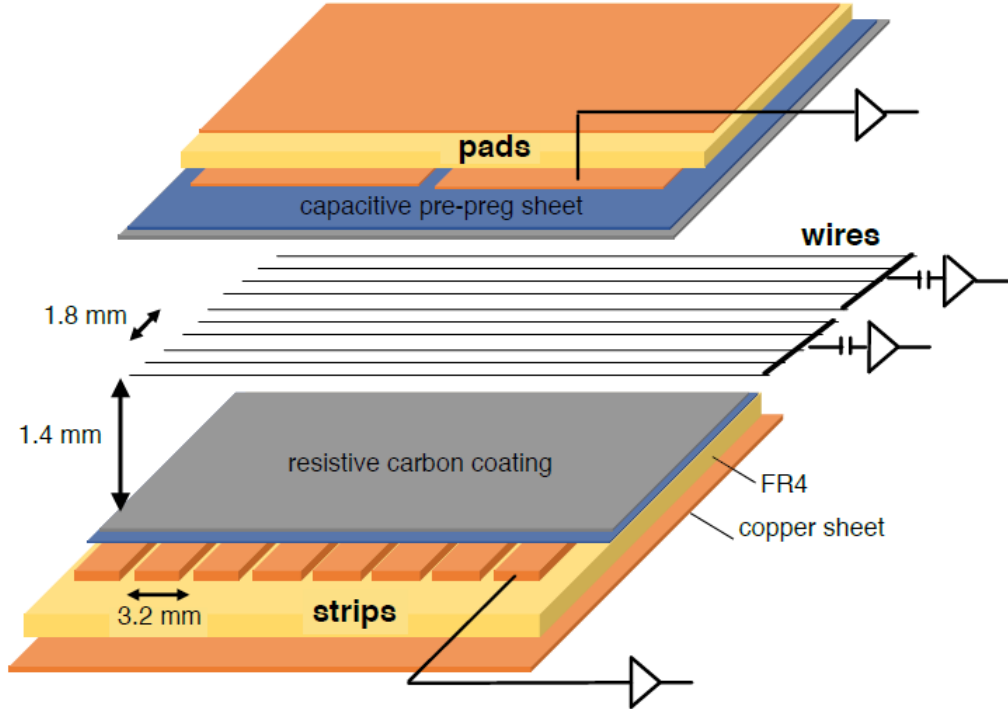


Figure 4.3: Internal structure of an sTGC, zoomed into the area under a pad. High voltage is applied to wires suspended in the gas volume to create an electric field. A passing muon causes an ionization avalanche that is picked up by the wire, strip and pad electrodes [8].

4.3 Small-strip thin gap chambers

The sTGCs are gas ionization chambers operated with a gas mixture of CO₂:n-pentane with a ratio of 55%:45% by volume. Gold-plated tungsten wires, 50 μm in diameter and with 1.8 mm pitch, are suspended between two cathode planes made of FR-4, each 1.4 mm away (see figure 4.3). One cathode board is segmented into copper pads of varying area (with a typical size of $\sim 300 \text{ cm}^2$ each), and the other is segmented into copper strips of 3.2 mm pitch running lengthwise perpendicular to the wires. High voltage is applied to the wires and the cathode planes are grounded [5, 53]. When a muon passes through a sTGC, it will ionize some of the atoms in the gas and the electric field in the gas gap will result in the formation of an ionization avalanche [54]. The motion of the ions and free electrons generates small currents on the nearby wire and capacitatively-coupled strip and pad electrodes [5]. The gas

509 mixture was chosen to absorb excess photons produced in the avalanche that delocalize the
510 avalanche signal [55] preventing the formation of streamers [42]. This allows the chamber to
511 be run at a higher high-voltage providing a faster response and higher signal. The resistivity
512 of the carbon coating and capacitance of the pre-preg sheet tune the spread of the charge
513 distribution [56] and the speed of the response [57] to optimize the rate capability. The
514 combined information from the strip readout electrodes and wires provide the location where
515 the muon passed through the chamber. The small pitch of the strip readout electrodes is
516 what allows the quadruplets to deliver good track angular resolution to improve the fake
517 trigger rate and meet the precision tracking requirements [5].

518 A 3-out-of-4 coincidence in pad electrodes from each layer of a quadruplet defines a region of
519 interest where the strip and wire electrodes should be read out. The pad triggering scheme
520 greatly reduces the number of electrodes that require readout so that a track segment of the
521 required angular resolution can be provided quickly enough to the hardware trigger [5].

522 Signal is read out from groups of successive wires, so the position resolution in the direction
523 perpendicular to the wires is 10 mm per plane. The wires give the azimuthal coordinate
524 in ATLAS so the position resolution in this direction is sufficient. Good resolution on the
525 η coordinate, perpendicular to the strips, is important [5]. In a test beam environment,
526 the strip spatial resolution of a single sTGC was measured to be 45 microns for muon
527 perpendicularly incident on the surface of the sTGC. Although the spatial resolution worsens
528 as function of muon angle measured from normal incidence [58], when four sTGCs are glued
529 together into a quadruplet the design angular resolution of 1 mrad in the strip coordinate is
530 achievable [5, 53].

531 To achieve the required track angular resolution once installed in ATLAS, the absolute
532 position of each sTGC strip within the ATLAS coordinate system must be accurately known.
533 The degree of accuracy required is on the order of the position resolution of the chambers,
534 $\sim 100 \mu\text{m}$. The NSW alignment system, detailed in section 4.5, will monitor the position of
535 alignment platforms installed on the surface of the wedges. The alignment platforms are
536 installed with respect to an external reference on the sTGCs: two brass inserts on each strip
537 layer on one of the angled sides of each quadruplet (shown in figure 4.4). So the challenge
538 of monitoring the position of the strips in ATLAS was separated into two steps: first, infer
539 the position of the strips with respect to the brass inserts using the sTGC design geometry;
540 second, use the alignment system to monitor the position of the alignment platforms. The
541 next section provides some pertinent details on the sTGC construction process, with steps
542 that affect the position of the strips with respect to the brass inserts highlighted.



(a) Brass insert near long edge.

(b) Brass insert near short edge.

Figure 4.4: The brass inserts sticking out from the gas volumes of an sTGC quadruplet. These inserts were pressed against alignment pins when the individual sTGCs were being glued together.

543 4.4 sTGC Quadruplet Construction

544 Five countries were responsible for producing sTGC quadruplets of varying geometries for the
545 NSW: Canada, Chile, China, Israel and Russia. Canada was responsible for the construction
546 of one quarter of the required sTGCs, of three different quadruplet geometries. The steps of
547 the construction process in each country were similar [5]. The process followed in Canada is
548 detailed here.

549 A research group at TRIUMF in Vancouver, British Columbia was responsible for preparing
550 the cathode boards. The boards were made and the electrodes etched on at a commercial
551 laboratory, Triangle Labs, in Carson City, Nevada. Once completed they were sent to TRI-
552 UMF to be sprayed with graphite and to have support structures glued on [7]. The boards
553 are commercial multilayer printed circuit boards, but the strip boards required precision ma-
554 chining to etch the strip pattern [5]. Triangle Labs also machined the two brass inserts into
555 each strip board. A coordinate measuring machine (CMM) was used to accurately measure
556 the position of a set of reference strips on each board. Four quality parameters describing
557 non-conformities in the strip pattern of each board with respect to the brass inserts were
558 derived from the data and the results are available on a QA/QC database. The parameters –
559 offset, angle, scale and nonparallelism – and the CMM data collection is described in full
560 in [7]. Due to time constraints, tolerances on the non-conformities in the etched strip pattern
561 with respect to the brass inserts were loosened, with the condition that the strip positions
562 in ATLAS would have to be corrected for [7].

563 The prepared boards were sent to Carleton University in Ottawa, Ontario for construction
564 into sTGCs and quadruplets. First, the wires were wound around the pad cathode boards
565 using a rotating table and the wires were soldered into place. A wound pad cathode board glued
566 on top to create an sTGC. Holding one sTGC flat with the vacuum, another was glued on
567 top to create a doublet, then two doublets were glued together to create a quadruplet. When
568 gluing sTGCs together, the brass inserts were pushed against alignment pins with the goal of
569 keeping the strip layers aligned within tolerance. However, non-conformities in the shape of
570 the brass inserts, non-conformities in the position of the alignment pins and shifts between
571 sTGCs while the glue cured resulted in misalignments between the brass inserts and strip
572 layers. Precise alignment of the pad boards or wires with respect to the strip boards did
573 not have to be so tightly controlled because pads and wires do not measure the precision
574 coordinate.

576 The Carleton team finished the quadruplets by installing adaptor boards on the angled sides
577 of each layer that allow front end electronics to be attached. Completed quadruplets were
578 sent to McGill University where their performance was characterized with cosmic rays. De-

579 tails pertaining to cosmic ray testing of sTGC quadruplets at McGill University are described
580 in chapter 5. Tested quadruplets were sent to CERN where they were assembled into wedges
581 and alignment platforms installed. The alignment platforms were installed using a jig posi-
582 tioned with respect to the brass inserts. Completed wedges were assembled into sectors then
583 installed on the NSWs.

584 The quadruplet construction process had two steps where strip positions could be shifted off
585 of nominal. At board-level, there could be non-conformities in the etched strip pattern with
586 respect to the brass inserts, described by the four quality parameters [7]. At the quadruplet
587 level, misalignments between the brass inserts and strips on different layers were possibly
588 introduced during the gluing. The result was that the brass inserts were not a reliable
589 reference point and that the strips can be offset from their design position by up to hundreds
590 of micrometers. Offsets in strip positions from nominal in Canadian quadruplets were shown
591 to be random [7], so no one correction would suffice. The offsets must be measured and
592 corrected for in the ATLAS offline software that does the precision tracking. Understanding
593 the work ongoing to make measurements of strip position offsets and correct for them requires
594 understanding the strategy of the NSW alignment system.

595 4.5 NSW alignment

596 The idea of the NSW alignment system is presented in [5], but the details have only been
597 presented internally so far. After the wedges are constructed, alignment platforms are in-
598 stalled on every sTGC quadruplet and optical fibres routed to them, as shown in figure 4.5.
599 Light from the optical fibres will be monitored in real time by cameras (BCAMs) mounted on
600 the alignment bars of the NSWs. The system will thus record the positions of the alignment
601 platforms in the ATLAS coordinate system and any changes over time.

602 The original alignment scheme was to use the brass inserts as a reference between the align-
603 ment platforms and the individual strips, as shown in the solid arrows in figure 4.6 – this
604 will no longer work. The position of the alignment platforms will be known thanks to the
605 alignment system, so a different method to get the position of the strips with respect to the
606 alignment platforms is currently in its final stage of development. The technique consists of
607 the measurement of the strip pattern offset at a few areas on the surface of a sTGC quadru-
608 plet using an xray gun mounted on the alignment platforms. The local strip pattern offset
609 with respect to nominal geometry at the location of each alignment platform is obtained
610 by analyzing the xray gun beam profile. As shown in figure 4.6, this approach essentially
611 bypasses the need to know the position of strips with respect to the brass inserts. The align-
612 ment platforms provide the link to the nominal geometry because the nominal group of strips

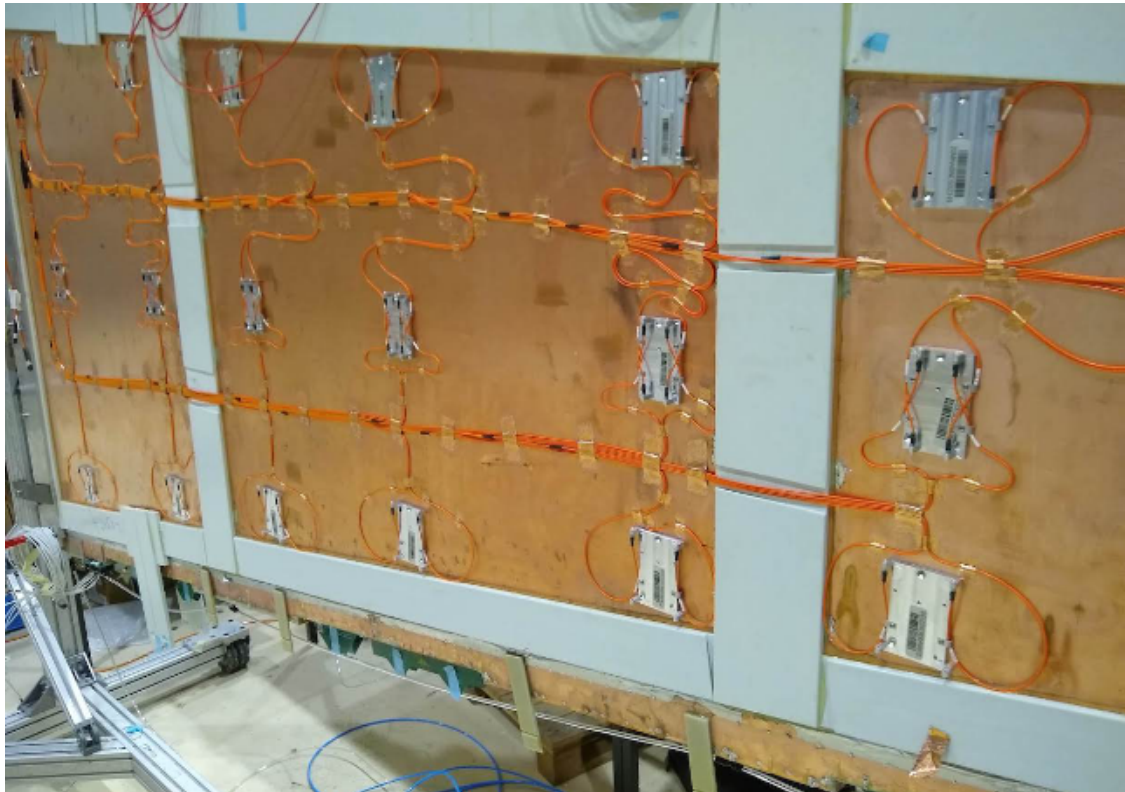


Figure 4.5: A sTGC wedge with alignment platforms (silver) installed on the quadruplet. Optical fibres (orange) are routed to the alignment platforms. Cameras on the frames of the NSWs will record light from the optical fibres to monitor in real-time the position the alignment platforms in the ATLAS coordinate system.

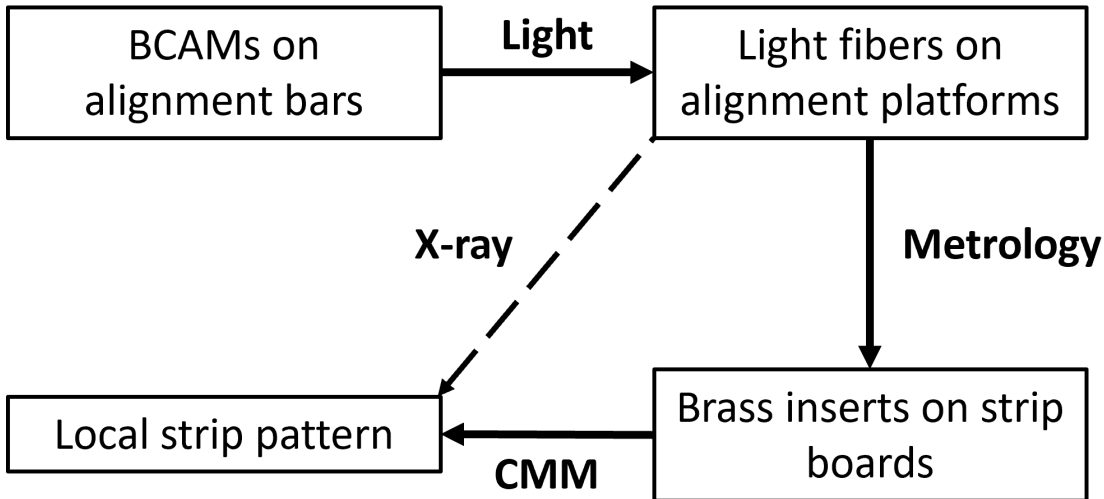


Figure 4.6: Schematic diagram showing how the different elements of the sTGC alignment system relate to one another. The solid arrows denote the planned alignment scheme. The dashed arrow shows the modification being finalized now. This figure was originally designed by Dr. Benoit Lefebvre.

613 that should be nearest to them can be identified using the nominal geometry parameters that
 614 assume the strips are perfectly etched and aligned. Cosmic muon track positions cannot be
 615 compared to the nominal geometry because the alignment platforms are not installed when
 616 cosmics data is collected, so there is no external reference to provide a link to the nominal
 617 geometry.

618 The x-ray method does not have the sensitivity to measure the offset of each strip from
 619 nominal, but what can be measured instead is the offset of the strip pattern in a local area
 620 around the position of the gun. *Local offsets* are used to build an alignment model for each
 621 strip layer. Formally defined, an alignment model is a set of parameters used to estimate the
 622 “as-built” position of a strip given its nominal position. The alignment model currently being
 623 worked on takes x-ray and CMM data as input to calculate an overall offset and rotation of
 624 each strip layer with respect to nominal [8]. The alignment parameters could be described
 625 as “global”, meaning over the whole layer instead of local. Without the x-ray dataset, there
 626 would be no input to the alignment model that takes into account inter-layer misalignments
 627 introduced during quadruplet construction.

628 Given that the x-ray local offsets can only be measured at positions where the gun can
 629 be attached and that they are an important part of the alignment scheme, the new x-ray
 630 measurement technique needs to be validated. The goal of this thesis is to validate the x-ray

631 local offsets while exploring how cosmics data complements and adds to the understanding
632 of strip positions and global alignment.

633 Chapter 5

634 Using cosmic muons to measure 635 relative strip position offsets

636 At McGill, among other quality and functionality tests, each Canadian-made quadruplet was
637 characterized with cosmic muons. In this chapter, the experimental setup and how the data
638 was analyzed to provide relative strip position offsets is presented. The analysis method
639 was motivated by the how it could be compared to data collected with the x-ray method
640 (chapter 6) but also stands alone as a characterization of the alignment between strips of
641 different layers. First, a brief introduction to cosmic rays.

642 5.1 Cosmic rays

643 The Earth is being bombarded by particles from the sun, galactic sources and extra galactic
644 sources – collectively called cosmic rays [19, 11]. Cosmic rays are mostly protons, but also
645 heavier ions, gamma rays and the term sometimes includes neutrinos. The primary (initial)
646 cosmic ray interacts with the atmosphere causes electromagnetic and hadronic showers of
647 particles. Hadronic showers result from the primary cosmic ray interacting strongly with the
648 target of the atmosphere and the most abundant products are pions. Charge pions mostly
649 decay to muons (there is a lesser contribution to the muon flux from kaons as well) [59].
650 Thanks to time dilation extending the muon’s lifetime as measured on Earth, a flux of
651 approximately 1 muon/cm²/ min reaches the ground [11]. Measuring the muon flux and
652 energy spectrum reveals information about primary cosmic rays [59] which is interesting to
653 high energy physicists and astrophysicists. The muon flux is also terribly convenient for
654 testing muon detectors.

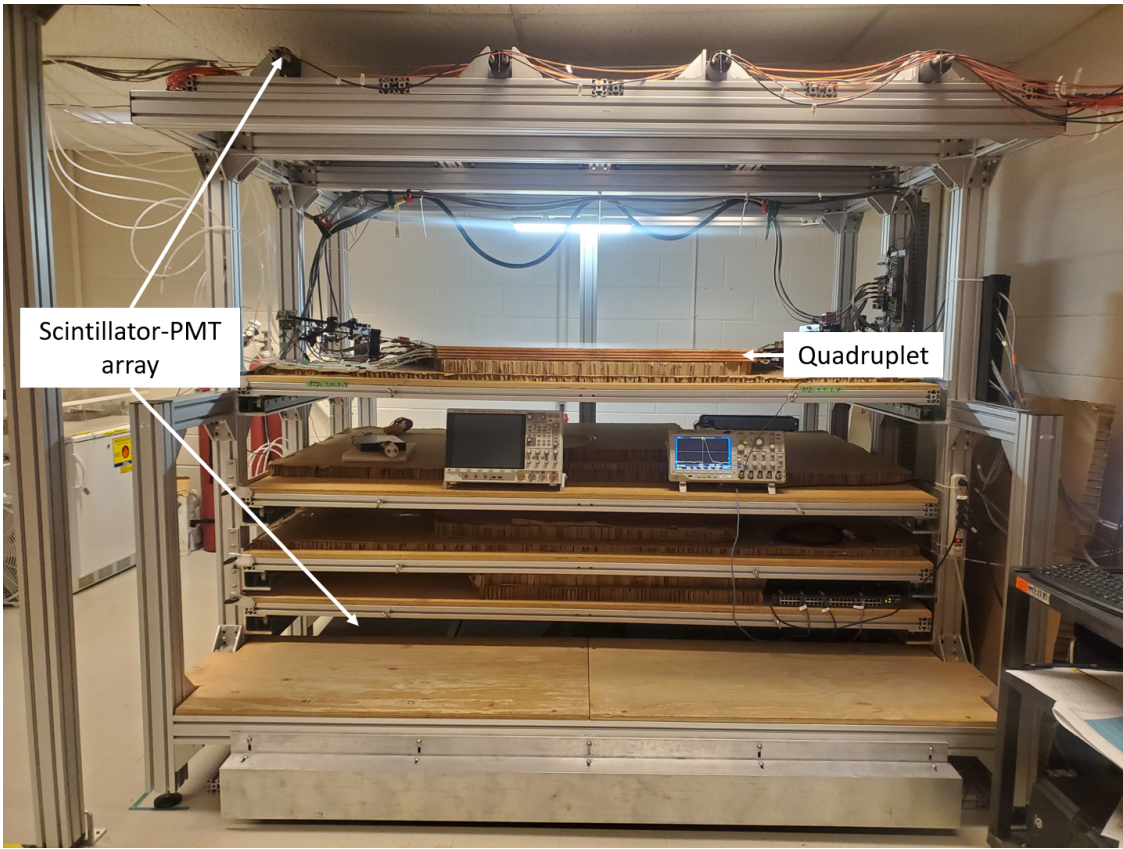


Figure 5.1: Cosmic muon hodoscope at McGill University with sTGC quadruplet in the test bench.

655 5.2 Experimental setup

656 Cosmic muon characterization was done with a hodoscope, a complete description of which
 657 can be found in [58]. The quadruplet was placed in the center of the test bench. Above
 658 and below it was a layer of scintillator-PMT arrays, labeled in figure 5.1. When a cosmic
 659 muon passed within the acceptance of the hodoscope, at least one scintillator from the top
 660 array and at least one from the bottom array fired in coincidence. The coincident signal was
 661 used to trigger the readout of the quadruplet's electrodes using NIM modules. The trigger
 662 was passed to the front-end electronics attached to the adaptor boards of each layer of the
 663 quadruplet.

664 Operating the chambers also required gas and high voltage. A pentane-CO₂ mixture was
 665 mixed and delivered to each sTGC with a gas system designed and made at McGill University.

666 The gas system was controlled by a slow control program, also made in-laboratory [60].
667 Although gas mixture is flammable, it allows the chambers to operate in high amplification
668 mode without production of excess photons saturating the signal across many strips because
669 pentane absorbs a wide energy of photons [55]. To prepare the quadruplets for operation,
670 CO_2 was flushed through them overnight to remove impurities. Then, five gas volumes of
671 the pentane- CO_2 mixture was flushed through (approximately 3 hours). High voltage was
672 provided by CAEN boards.

673 5.3 Data acquisition

674 Each sTGC electrode was connected to a channel on a prototype ASIC¹ on the front-end
675 electronics, attached to the adaptor boards on each layer of a quadruplet. The ASIC ampli-
676 fied the signal and was set to measure and record the signal peak amplitude from electrodes.
677 For each trigger, the signal peak amplitude of all channels above threshold was recorded
678 as an event and stored in a binary file. Channel thresholds were estimated [62] and ad-
679 justed manually in the configuration/readout software before the start of data acquisition.
680 There was an exception to the threshold rule: the signals on strips adjacent to a strip above
681 threshold were also readout using the so-called “neighbour triggering” function of the ASIC.
682 The quadruplets were held at 3.1 kV for approximately two hours to collect data from 1
683 million muon triggers.

684 5.4 Data preparation

685 5.4.1 Cuts on electrode hits

686 Corrupted data is removed while the raw data is being recorded in a binary file. The binary
687 file is decoded into a usable ROOT [63] tree offline.

688 A hit is defined as a signal recorded from a channel that was above threshold or (in the
689 case of strips) neighbour triggered. In addition to hits from muons, the quadruplets record
690 noise from the electronics and δ -rays (electrons liberated with sufficient energy to cause more
691 ionization before acceleration). Therefore, cuts are applied to reduce the number of noise
692 hits. The edge strips are very noisy, so all strip hits on layers with strip hits on either
693 edge channel are cut. A default pedestal value is subtracted from the recorded signal peak

¹the VMM3 [61], designed for the MMs and sTGCs of the NSW

694 amplitude of each electrode for a more realistic estimate of the signal amplitude. Also, events
695 that only have hits on pad electrodes (no strips or wires) were cut because the large area of
696 the pads made them susceptible to noise.

697 **5.4.2 Clustering and tracking**

698 Many of the high-level characterization metrics require rebuilding muon tracks. For events
699 passing quality cuts, the x - and y -coordinates of the ionization avalanche on each layer are
700 extracted from the signal on the wires and strips respectively for each event, as is sketched in
701 figure 5.2. In this work, x is the coordinate perpendicular to the wires and y is the coordinate
702 perpendicular to the strips.

703 The x -coordinate is taken as the center of the wire group with the maximum peak signal
704 amplitude, since the wire groups' pitch (36 mm) is larger than the typical charge spreading.
705 Assuming that the true x -position of the hit is sampled from a uniform distribution over the
706 width of the wire group, the uncertainty in the x -position was given by $\frac{36}{\sqrt{12}}$ mm = 10 mm [64].

707 The y -coordinate is taken as the Gaussian mean of the peak signal amplitude distribution
708 across groups of contiguous strips. The process of grouping contiguous strip hits on a layer is
709 called clustering, and the resulting group is called a cluster. Figure 5.2 sketches the clustering
710 process and a sample cluster is shown in figure 5.3. The data acquisition system recorded
711 the electrode ID of the strip hit and in the clustering process the position of the center
712 of the strip electrode is calculated based on the nominal quadruplet geometry. Typically,
713 clusters are built of 3-5 strips. The thickness of the graphite coating over the cathode boards
714 determined how many strips picked up the ionization image charge. Larger clusters were
715 more likely caused by δ -rays since they spread the cloud of ionization.

716 Events are cut from the analysis if there are two clusters on one layer's set of strips (indicative
717 of noise). Clusters are cut if the cluster size is lesser than three (which should not happen for
718 real events thanks to neighbour triggering), and if the cluster size is greater than 25. After
719 all the cuts on hits and clusters, roughly half as many muon tracks as triggers collected
720 remain.

721 The uncertainty in the y -coordinate could have been taken as the fitted cluster mean's
722 statistical uncertainty; however, after comparing the difference in cluster means for different
723 fitting algorithms in appendix A.2, 60 μm of uncertainty was assigned.

724 The coordinates of the avalanches' on all layers were used to reconstruct tracks in x and y
725 respectively. The tracks were then used to calculate characterization metrics like electrode
726 efficiency and spatial resolution, the details of which are discussed in [58].

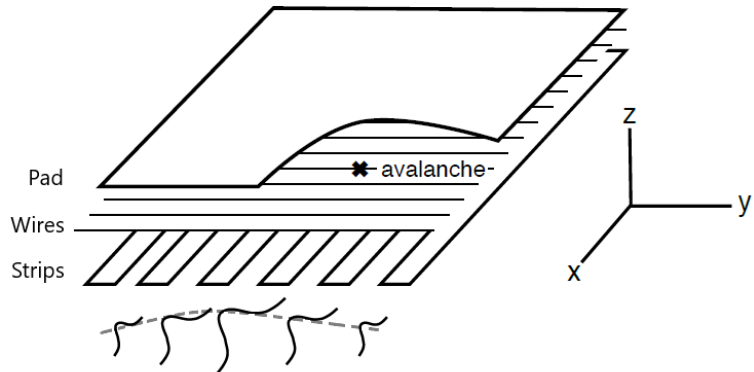


Figure 5.2: A sketch of an sTGC-like detector. The position of the avalanche is extracted from the wires and strips that picked up the avalanche signal. The signals on individual strips are sketched. Clustering was the processs of fitting a Gaussian to the peak value of the signals on individual contiguous strips, as is done in figure 5.3. In this work, the $x(y)$ -coordinate will always refer to the coordinate perpendicular to the wires (strips) [58, 56].

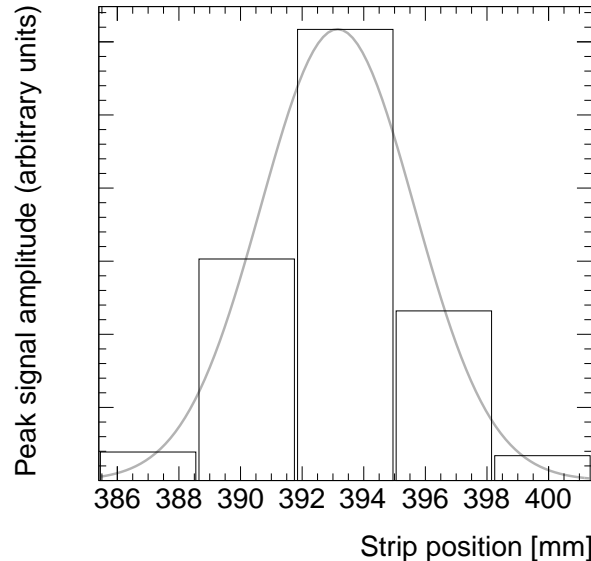


Figure 5.3: A sample cluster resulting from the current picked up on a group of strips after the passing of a muon (presumably). The grey curve is a Gaussian fit.

727 5.5 Measuring relative local offsets

728 The offset of a strip from its nominal position can be modeled as a passive transformation.
729 For each area of a strip layer, the local offset is the shift of the strip pattern in that area with
730 respect to the nominal geometry. Local offsets systematically change the set of strips nearest
731 to muons passing through the area. The data preparation software assumes that strips are
732 in their nominal positions, so the recorded muon y -position on layer i , y_i , is shifted opposite
733 to the layer's local offset, $d_{local,i}$, by

$$y_i = y_{nom,i} - d_{local,i}, \quad (5.1)$$

734 where $y_{nom,i}$ is the position of the muon that would have been recorded on layer i if there
735 was no local offset. Equation 5.1 ignores other factors that affect the cluster position, like
736 position resolution. With cosmics data, the local offset is unknown and there was no external
737 reference to measure $y_{nom,i}$. Therefore, only relative local offsets could be calculated.

738 The minimal relative coordinate system uses two reference or fixed layers [58]. The hits
739 on the two fixed layers were used to create tracks that can be interpolated or extrapolated
740 (polated) to the other two layers. The set of two fixed layers and the layer polated to are
741 referred to as a tracking combination. The residual of track i , Δ_i is defined as,

$$\Delta_i = y_i - y_{track,i}, \quad (5.2)$$

742 where $y_{track,i}$ is the polated track position. Track residuals are affected by the relative local
743 offset in the area of each layer's hit. As an example, in figure 5.4, the residual on layer
744 2 perhaps indicates that layer 2 is offset with respect to layers 1 and 4 in the area of the
745 track. Of course, a single track residual says nothing of the real relative local offset because
746 of the limited spatial resolution of the detectors and fake tracks caused by noise or delta
747 rays. However, the mean of residuals for all tracks in a region will be shifted systematically
748 by the local offsets between layers [58]. For a quadruplet with nominal geometry, the mean
749 of residuals should be zero in all regions and for all reference frames, unlike the example
750 regions in figure 5.5. The value of the mean of residuals is a measure of the relative local
751 offset of the layer with respect to the two fixed layers.

752 To study the relative local offsets, residual distributions across each strip layer of a quadruplet
753 for all tracking combinations were assembled and fitted. The residual distributions were
754 wider for tracking combinations where the extrapolation lever arm was largest, as in the
755 example distributions shown in figure 5.5. In general, residual means from distributions of
756 residuals with geometrically less favourable tracking combinations have larger statistical and
757 systematic uncertainties. The bin size of 200 μm for the distributions shown in figure 5.5 was

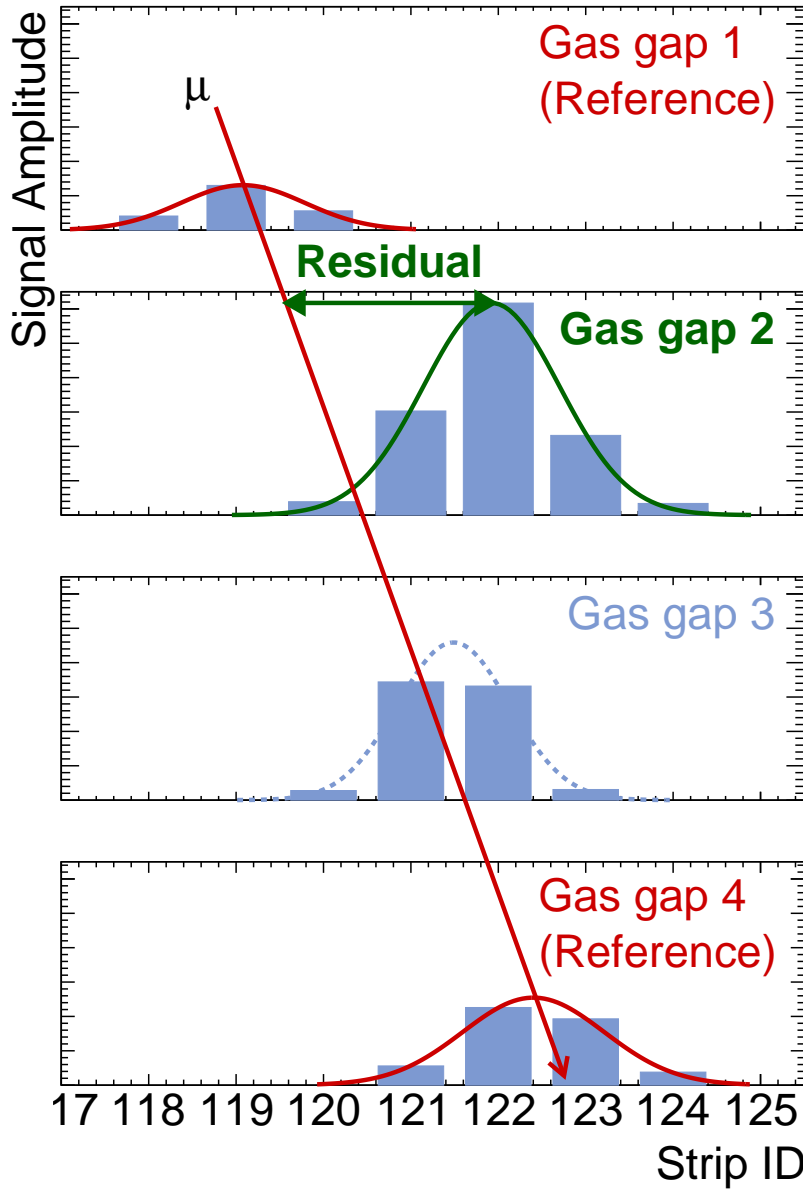
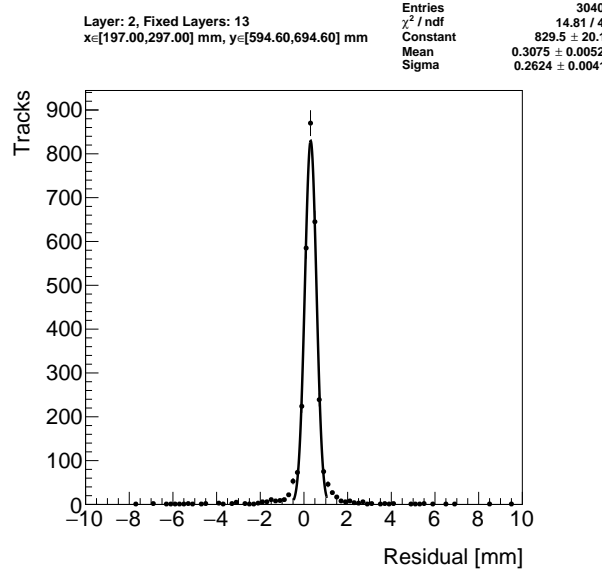
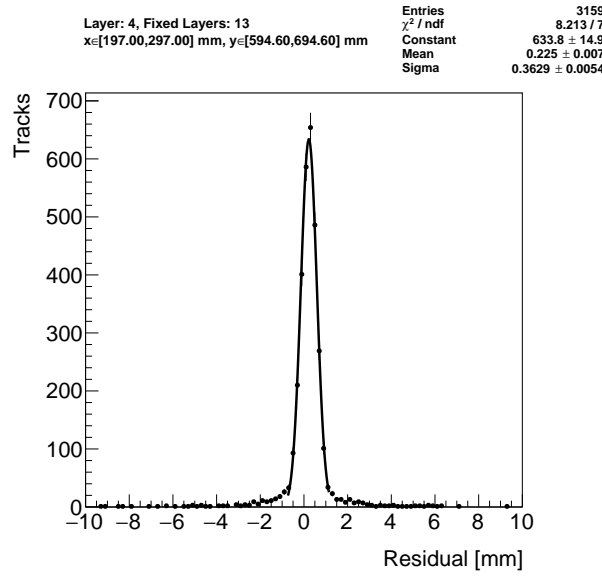


Figure 5.4: Representation of a muon event recorded by an sTGC. The clusters are fit with a Gaussian and the mean is taken as the hit position. A track is built from the chosen reference layers, 1 and 4, and the residual calculated on layer 2. The clusters come from a real muon, but their positions were modified to highlight the residual on layer 2.



(a) Tracks on layer 2, reference layers 1 and 3.



(b) Tracks on layer 4, reference layers 1 and 3.

Figure 5.5: Residual distribution in the region $x \in [197, 297]$, $y \in [594.6, 694.6]$ mm (100 mm by 100 mm area) for two different tracking combinations. Data from quadruplet QL2.P.11.

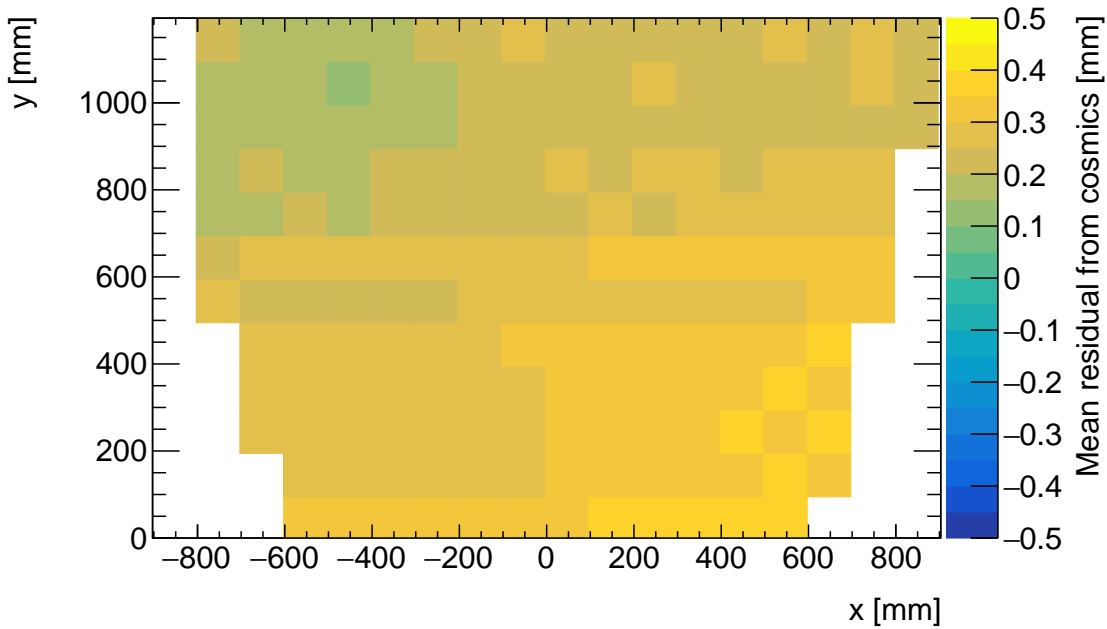
758 chosen based on the uncertainty on residuals calculated from tracks on layer 4 (1) built from
759 hits on layers 1 and 2 (3 and 4) given a cluster y -position uncertainty of $60 \mu\text{m}$ (appendix A.3),
760 since these tracks yield residuals with the largest uncertainties.

761 A gaussian fit was used to extract the mean of the residual distributions. Theoretically, a
762 double gaussian distribution is more apt, but for this analysis the gaussian fit was sufficient,
763 as discussed in appendix C.1.

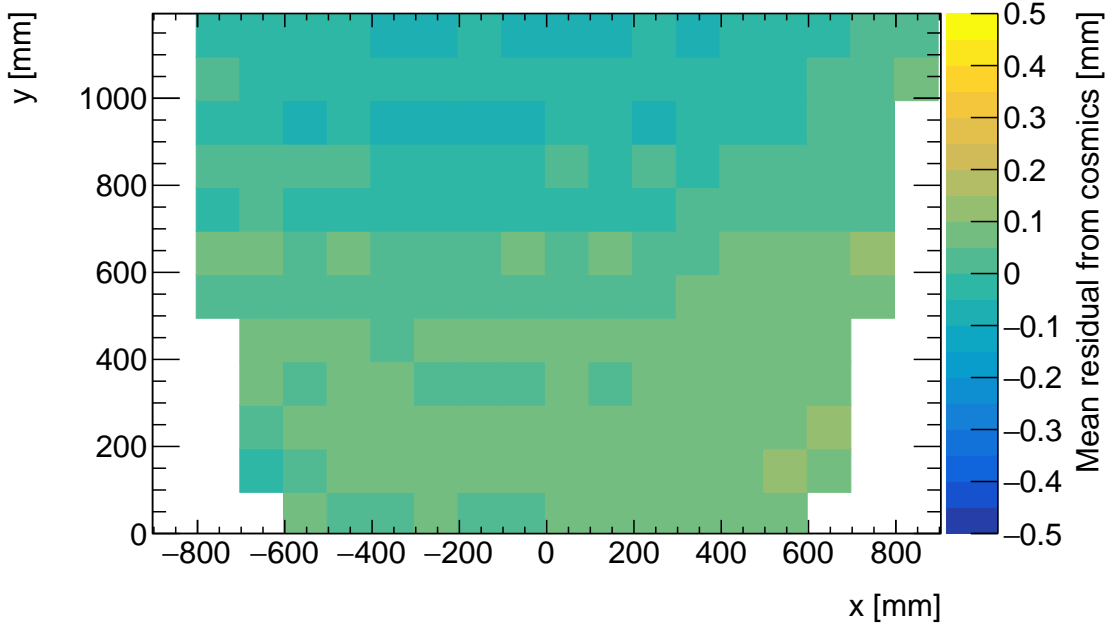
764 The area of the region of interest was 100 mm by 100 mm. The size balanced the amount of
765 tracks falling in the region of interest to give a small statistical uncertainty on the extracted
766 mean while being smaller than the order on which local offsets were expected to change
767 significantly. The change in local offsets over the surface of a layer can be modeled using
768 global alignment parameters. Using a base alignment model with a global offset and rotation
769 of each strip layer, “significantly” was defined by the distance in x that a large but possible
770 rotation of $1000 \mu\text{rad}$ would change the local offset by more than $50 \mu\text{m}$ – half the required
771 position resolution of the sTGCs [5].

772 5.6 Visualizing relative alignment between layers

773 The mean of residuals was plotted across entire strip layers for every tracking combination to
774 get a picture of the how relative local offsets change over the layers’ surface. Figure 5.6 shows
775 the mean of residuals on layer 2 with reference layers 1 and 3 for two different quadruplets,
776 referred to as QL2.P.11 and QL2.P.8, for 100 mm by 100 mm areas across the surface of
777 layer 2. To understand these plots, realize that the Gaussian mean of the distribution in
778 figure 5.5a is the entry in area bin $x \in [197, 297], y \in [594.6, 694.6]$ mm in figure 5.6a.



(a) Mean of residuals of tracks on layer 2, reference layers 1 and 3, for QL2.P.11.



(b) Mean of residuals of tracks on layer 2, reference layers 1 and 3, for QL2.P.8.

Figure 5.6: Mean of residuals in each 100 mm by 100 mm bin over the area of the layer 2 cathode board. The entry in $x \in [197, 297]$, $y \in [594.6, 694.6]$ mm of figure 5.6a corresponds to the fitted Gaussian means in figures 5.5a. The mean of residuals is an estimate of the local offset of layer 2 with respect to layers 1 and 3.

779 Many of the residual means are non-zero and change smoothly over the layer, indicating
780 that there are relative local offsets stemming from misalignments between entire strip layers.
781 Given that the residual mean changes with x in figure 5.6a, there is likely a rotation of layer
782 2 with respect to layers 1 and 3 on QL2.P.11, combined with an offset of the entire layer.
783 The residual means are smaller in figure 5.6b indicating that QL2.P.8 is less misaligned
784 overall than QL2.P.11; however the relative local offsets range between $\pm 200 \mu\text{m}$ so they are
785 still significant considering the order on which the chambers must be sensitive to position,
786 $\sim 100 \mu\text{m}$.

787 5.7 Systematic uncertainty

788 The statistical uncertainty on the local residual means was typically around $10 - 20 \mu\text{m}$, and
789 appendix B shows that the analysis was not statistically limited by the number of triggers
790 collected for each quadruplet. The systematic uncertainties were more significant.
791 Systematic uncertainties were assigned per tracking combination as the RMS of the dis-
792 tribution of the difference in local residual means each calculated in a different way. For
793 example, the RMS associated with fitting the local residual distributions with a Gaussian or
794 double Gaussian is $25 \mu\text{m}$ for the geometrically least favourable tracking combinations. The
795 distribution is shown in appendix C.1. For geometrically similar tracking combinations (like:
796 tracks on layer 1 built from hits on layers 3 and 4, and tracks on layer 4 built from hits on
797 layers 1 and 2), the systematic uncertainty was assigned as the average RMS of both.
798 Other choices were: whether to use data collected at 2.9 kV or 3.1 kV (both are collected
799 at McGill); what cluster fitting algorithm to use; and whether or not to apply a differential
800 non-linearity (DNL) correction to the cluster y -positions [6]. A systematic uncertainty was
801 assigned using the method above to account for the effect of each choice and quantify the
802 robustness of the mean of residuals. The reasons for each choice are listed below.
803 Data taken at 3.1 kV was used over 2.9 kV because the strip and wire tracking efficiency
804 increases with higher voltage [58] (appendix C.2).
805 The Minuit2 package [65] was used to fit clusters over Guo's method [66] because it provided
806 automatic statistical uncertainty estimates and is the standard fit algorithm of ROOT [63]
807 (appendix C.3).
808 The DNL correction was not applied because its effect on the residual means was negligible
809 (appendix C.4).
810 A summary of the systematic uncertainties assigned for each tracking combination is given
811 in table 5.1.

Tracking geometry	Residual distribution fit function (C.1)	Cosmics data collection voltage (C.2)	Cluster fit algorithm (C.3)	Apply DNL correction or not (C.4)	Total
Similar to layer 3, fixed layers 1, 2	0.01	0.04	0.02	0.01	0.05
Similar to layer 4, fixed layers 1, 2	0.03	0.01	0.03	0.01	0.10
Similar to layer 2, fixed layers 1, 3	0.01	0.02	0.01	0.000	0.03
Similar to layer 4, fixed layers 1, 3	0.01	0.04	0.01	0.01	0.04
Similar to layer 2, fixed layers 1, 4	0.01	0.04	0.01	0.01	0.04

Table 5.1: Systematic uncertainty assigned for each analysis option, detailed in appendix [C](#).

812 The uncertainty in each mean of residuals was assigned as the sum in quadrature of the sta-
813 tistical uncertainty in the mean and the appropriate systematic uncertainty for the tracking
814 combination.

815 5.8 Discussion

816 Cosmics data is being used to calculate relative alignment parameters using two other meth-
817 ods [58]. A cross-check of this analysis would be to compare their results; however the studies
818 in appendix C show that the mean cosmics residuals are robust, so the comparison was not
819 prioritized.

820 Given that the uncertainty in the residual means is lesser than or near to the order of the
821 required position resolution of the sTGCs (100 μm [5]) they are relevant input for alignment
822 studies.

823 The relative local offsets as calculated from the mean of residual distributions provide a
824 complete picture of the relative alignment between detectors planes. In fact, cosmic muon
825 testing is the only characterization technique where the entire surface of quadruplet layers
826 can be probed since muons hits are distributed almost uniformly; the CMM [7] and x-ray
827 methods [8] depend on measurements at reference points, and test beams only have a limited
828 beam spot [6]. By looking at 2D-histograms of residual means like figure 5.6 for all tracking
829 combinations, it is easy to identify quadruplets that suffer large relative misalignment since
830 many residual means differ significantly from zero. Moreover, the pattern in the relative
831 local offsets can be used to motivate a physical interpretation of misalignments. The relative
832 local offsets can be used as a reference, cross check, or input in other alignment studies.

833 Relative local offsets cannot be used to position strips in the absolute ATLAS coordinate
834 system because there was no external reference to measure positions on all layers with re-
835 spect to. The lack of external reference means that there is not enough information to unfold
836 relative local offsets into absolute local offsets (with respect to the nominal quadruplet ge-
837 ometry). As an example, assuming that the residual on layer 2 in figure 5.4 is representative
838 of the relative local offset, the residual on layer 2 could be caused by the strips on layer 2
839 being misaligned from nominal, but it could also be caused by strips on layers 1 and 4 being
840 offset from nominal while the strips on layer 2 are in their nominal positions! Any number
841 of combinations of local offsets on layers 1, 2 and 4 could produce the residual on layer 2.
842 Absolute local offsets must be calculated another way.

843 **Chapter 6**

844 **Using x-rays to measure relative strip
position offsets**

846 Local offset measurements were done with the x-ray method. The reader is referred to the
847 paper describing the x-ray method [8], although some minor changes have been made to the
848 experimental setup since it was written. The experimental setup described here is current
849 and was used to collect the data presented in this thesis.

850 **6.1 Experimental setup**

851 The x-ray tests were performed after the quadruplets arrived at CERN, were assembled into
852 wedges, and alignment platforms installed. Essentially, an x-ray gun was attached to one
853 of the alignment platforms glued to the surface of the wedge and the x-ray beam profile
854 recorded by the strips.

855 The wedges were installed on carts that could rotate their surface to a horizontal position. A
856 mounting platform was installed on top of the alignment platform using a three-ball mount.
857 The x-ray gun used was an [Amptek Mini-X tube](#). The gun was placed in a brass holder
858 with built-in 2 mm collimator and 280 μm copper filter. The holder was mounted on one
859 of five positions on the mounting platform, as shown in figure 6.1. Gun positions were
860 chosen to avoid wire support structures in the sTGCs that reduce hit efficiency [58] and
861 boundaries between sets of strips read out by two different ASICs that could each have
862 different thresholds.

863 As with cosmics data collection, each sTGC also needed gas and high voltage to operate.

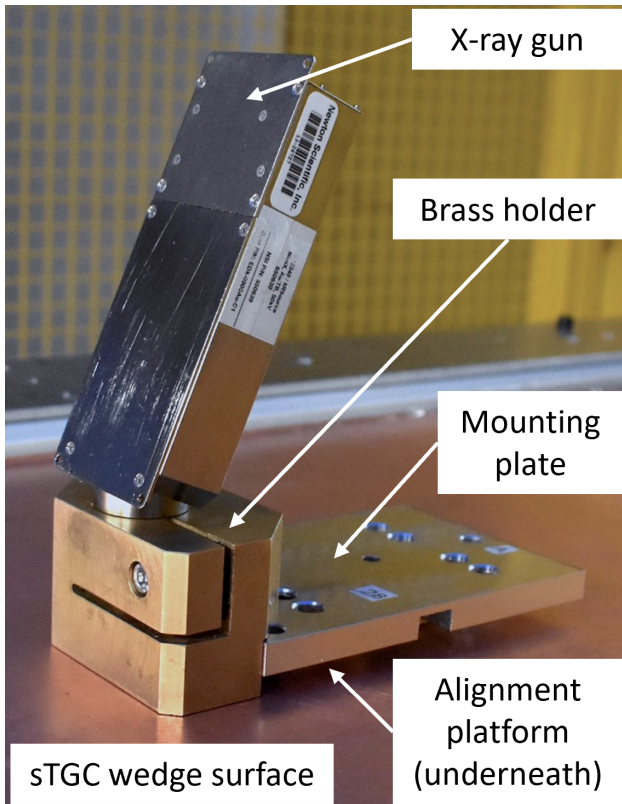


Figure 6.1: The x-ray gun mounted to the alignment platform on the surface of the wedge.
Adapted from [8].

864 Each layer was operated at 2.925 kV with high voltage from a NIM crate. The chambers
865 were flushed with CO₂ before and during data collection.

866 The gun produced x-rays with energies under 40 keV with peaks in the 7-15 keV range. The
867 x-rays mostly interacted with the wedge's copper electrodes and gold-plated tungsten wires
868 via the photo effect. The resulting photoelectrons caused ionization avalanches that were
869 picked up by the strips.

870 6.2 Data acquisition

871 A different version of the same front end electronics, but the same ASIC, as used in cosmics
872 testing were used for the x-ray testing to amplify the data and measure the peak signal
873 amplitude. Data was collected for two minutes per gun position with random triggers. A
874 trigger recorded all signals above threshold. Pad and wire data was not recorded.

875 6.3 Data preparation

876 Like with cosmics analysis, a default pedestal is subtracted from the signal peak amplitude
877 on each electrode.

878 Clusters are defined as groups of contiguous strip hits collected within 75 ns. The peak signal
879 amplitude of each electrode in a cluster is fit with a Gaussian, and the mean of the Gaussian
880 is taken as the cluster position. Cluster positions are corrected for DNL (see definition in
881 appendix C.4). Only clusters composed of hits on 3-5 strips were used in the x-ray analysis.
882 Clusters with signal on more than 5 strips were cut because they were most likely caused by
883 photoelectrons ejected with enough energy to be δ -rays.

884 The x-ray analysis diverges entirely from the cosmics analysis algorithm here because the
885 x-rays do not leave tracks. The signals picked up by the strips are from photoelectrons
886 liberated from the metals of the sTGCs, which only travel through one gas volume and are
887 ejected at all angles. Instead of creating tracks, the cluster position distribution on each
888 layer is used to define the beam profile. A typical beam profile is shown in figure 6.2.

889 6.4 Measuring local offsets

890 The mean of the cluster position distribution is taken as the x-ray beam profile center.
891 The expected center is calculated assuming a wedge with nominal geometry given the gun

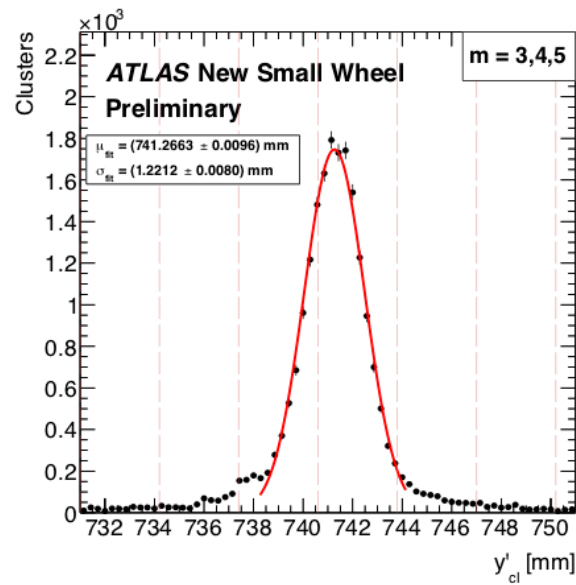


Figure 6.2: Distribution of x-ray cluster mean positions after the analysis cuts and corrections. The strip cluster multiplicity, m , was limited to 3, 4 and 5. The red curve is a Gaussian fit of the distribution and the pink dashed lines denote the edges of the strips [8].

position, corrected for: the geometry of the brass holder, the positioning and angle of the alignment platforms and the beam angle. The difference between the expected and reconstructed beam profile center is a measure of the local offset. Applying the logic of equation 5.1 to the beam profile, the Gaussian mean of cluster positions on the given layer acts as the recorded position, y_i , the expected center is $y_{nom,i}$ and the local offset is $d_{local,i}$ as before, where i denotes the layer. Since the position of the alignment platforms will be monitored by the alignment system in ATLAS [5], the position of the strips that should have been at the gun position are shifted by $d_{local,i}$ and so are known in the ATLAS coordinate system for every position where x-ray data was taken.

The x-ray working group accepted an uncertainty of 120 μm on the beam profile centers. The largest uncertainty comes from the effect of the gun angle, which proved difficult to measure and correct for.

The local offsets are not presented here as the author did not conduct this work. However, the author used the local offsets to calculate relative local offsets.

6.5 Measuring relative local offsets

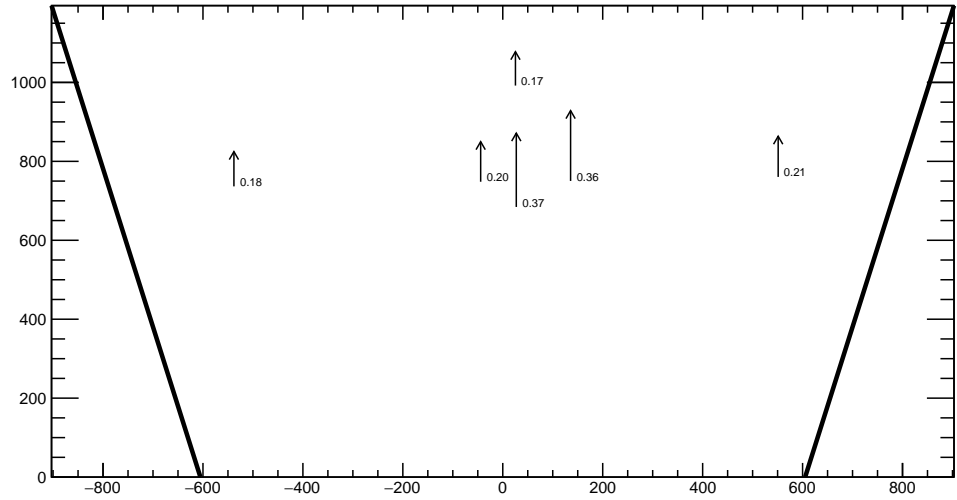
The x-ray local offsets were shown to be correlated with the local offsets calculated from the CMM data, but the CMM data does not include the effect of inter-layer misalignments so the degree of correlation measurable was limited. Cosmics data is affected by inter-layer misalignments. Since the local offsets for x-rays and cosmics data are measured in different coordinate systems, they cannot be compared directly. Bringing the cosmics relative local offsets into an absolute coordinate system is impossible; however, the x-ray local offsets can be brought into a relative coordinate system.

The measured x-ray beam profile centers were systematically affected by local offsets in the same way as the mean cosmics residuals, as modeled by equation 5.1. Therefore, if a 2-layer track is built from the beam profile centers on each layer and the residual calculated on a third layer, that residual should match the local mean cosmics residual. The residual is the difference between the beam profile center on the layer of interest and the polated track position from the beam profile centers recorded on the two fixed layers. The beam profile center on the layer of interest acts as y_i and the polated track position acts as $y_{track,i}$ in equation 5.2.

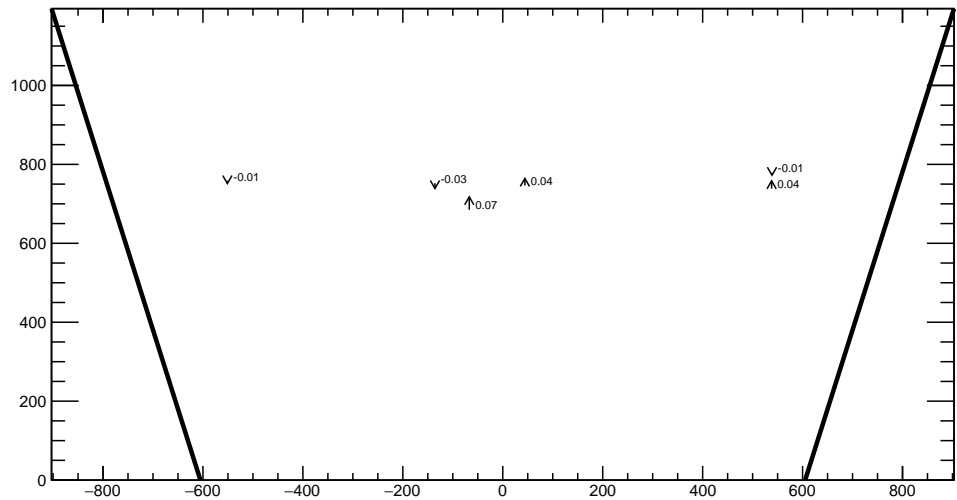
The built track is not an actual track of the x-ray beam. A beam profile center is actually the Gaussian mean of all selected mean cluster positions recorded during the x-ray data taking period, not a single hit of a track. Building an “abstract” track was necessary because

925 the x-rays cause signal in the chamber via the photoeffect so there were not individual “x-
926 ray tracks” to record. In fact the x-ray data could be collected separately for each layer.
927 Nonetheless, since the effect of local offsets on the beam profile centers was the same as their
928 effect on the recorded cosmics cluster positions the difference in algorithm between x-ray
929 and cosmics analysis was allowed.

930 For each x-ray survey position, the x-ray residual was calculated for all possible tracking
931 combinations (which required an x-ray beam profile on at least three layers). The x-ray
932 residuals on layer 2 calculated from the beam profile centers recorded on layers 1 and 3 are
933 represented as arrows in figure 6.3 as arrows for QL2.P.11 and QL2.P.8. For QL2.P.11, a
934 negative offset at all x-ray survey positions is clear.



(a) QL2.P.11 x-ray residuals on layer 2, reference layers 1 and 3.



(b) QL2.P.8 x-ray residuals on layer 2, reference layers 1 and 3.

Figure 6.3: The x-ray residuals on layer 2 calculated from the beam profile centers recorded on layers 1 and 3 for QL2.P.11 and QL2.P.8. The arrows originate from the expected position of the beam profile center assuming a nominal geometry, and the lengths are proportional to the calculated x-ray residuals. The tip of the arrow represents where the recorded hit was with respect to where it should have been recorded nominally. The value of the x-ray residuals are annotated in millimeters and have an uncertainty of ± 0.15 mm.

935 The uncertainty on the x-ray residuals was the error propagated through the tracking, taking
936 an uncertainty of 120 μm on each beam profile center. The uncertainty on the x-ray residuals
937 ranged from 0.15 mm to 0.4 mm from the most to least geometrically-favourable tracking
938 combination. There is no discernible pattern to the x-ray residuals on QL2.P.8 because they
939 are smaller than the uncertainty. The x-ray residual uncertainties are significantly larger
940 than the uncertainties on the relative local offsets calculated with cosmics data.

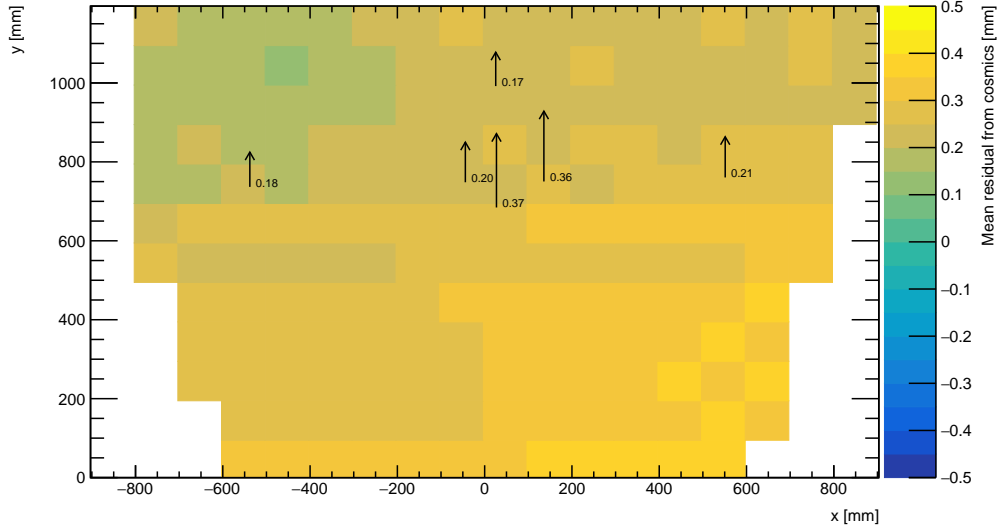
941 **Chapter 7**

942 **Comparing cosmic muon and x-ray
943 relative strip position offsets**

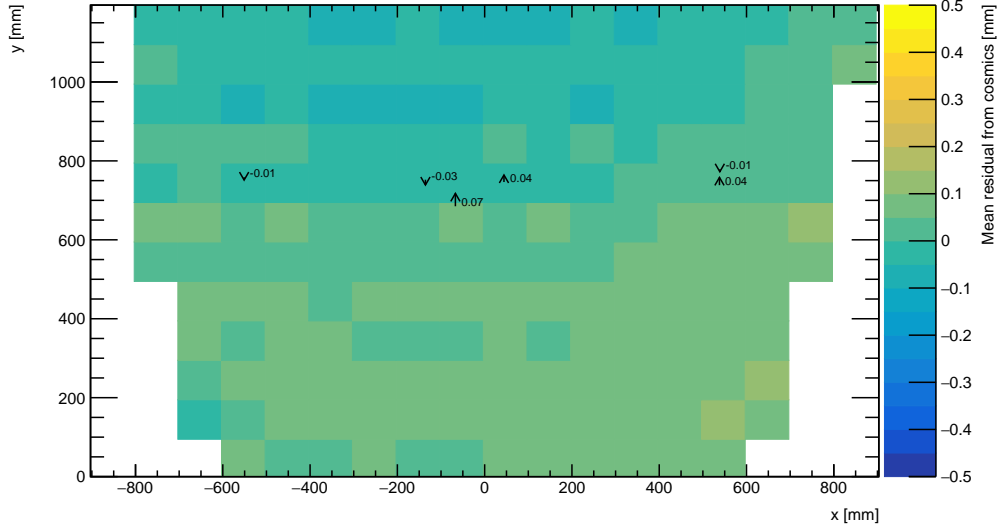
944 The goal was to validate the local offsets extracted from the x-ray data with cosmics data.
945 The complication was that the x-ray dataset provided absolute local offsets while the cosmics
946 dataset provided relative local offsets, which could not be compared directly. The solution
947 was to use the x-ray local offsets to calculate relative local offsets. The x-ray relative local
948 offset is the x-ray residual reconstructed from an abstract track using the beam profile
949 centers on each layer as the track hits. The cosmics relative local offset was taken as the
950 Gaussian mean of muon track residuals in a 100 mm by 100 mm area, referred to as the
951 mean cosmics residual. Relative local offsets of each type calculated using the same
952 reference layers are compared for each area where x-ray data is available. The results of the
953 comparison are presented here.

954 **7.1 Assessing correlation**

955 The 2D visualizations of the mean cosmics and x-ray residuals for tracks on layer 2 with
956 reference layers 1 and 3 on QL2.P.11 and QL2.P.8 are shown in figure 7.1. Figure 7.1 is a
957 superposition of figures 5.6 and 6.3.



(a) QL2.P.11 residuals of tracks on layer 2, reference layers 1 and 3.



(b) QL2.P.8 residuals of tracks on layer 2, reference layers 1 and 3.

Figure 7.1: The mean cosmics residuals are shown using colour. The x-ray residuals available at nominal gun positions are drawn as arrows and the value of the residual annotated in millimeters with uncertainty ± 0.15 mm. The length of the arrows is 500 times the value of the x-ray residual, scaled for visibility. These plots are a superposition of figures 5.6 and 6.3.

958 Figure 7.1a shows that for QL2.P.11 the x-ray residuals are of the same sign and order as
959 the mean cosmics residuals, as can be seen by comparing the the annotated value of the
960 x-ray residual to the mean cosmics residual represented by colour; QL2.P.11's mean cosmics
961 and x-ray residuals are correlated to some degree. For QL2.P.8, the x-ray residuals are of
962 the right order compared to the mean cosmics residuals, but the correlation is less apparent.
963 While x-ray residuals do not reveal a pattern across the layer's surface, the mean cosmics
964 residuals show a structure to the relative local offsets since they vary smoothly over the
965 surface of layer 2.

966 The comparison of mean cosmics and x-ray residuals was done for several quadruplets for
967 all tracking combinations (not just layer 2 residuals calculated with fixed layers 1 and 3 like
968 in figure 7.1). Scatter plots of the x-ray and mean cosmics residuals on QL2.P.11 and -2
969 for all tracking combinations shown in figures 7.2 and 7.3 reveal the degree of correlation
970 between the datasets. In the correlation plots, each rectangle is centered on the value of a
971 mean cosmics and x-ray residual pair calculated with a given tracking combination for every
972 gun position where data is available; the height and width of the squares are the uncertainty
973 in the mean cosmics and x-ray residuals respectively. Note that in the scatter plots, the
974 regions of interest where cosmics tracks are included in the calculation of mean of residuals
975 are exactly centered on the nominal x-ray beam position, unlike in figure 7.1.

976 The fitted slope and offset in figure 7.2 show that the two QL2.P.11 datasets are correlated.
977 The large uncertainty on the x-ray residuals set a limit on the sensitivity of the analysis,
978 for if the absolute value of the x-ray residuals of a quadruplet were smaller than the x-ray
979 residual uncertainties, no conclusion about the correlation could be drawn, like for QL2.P.8
980 (figure 7.3). This result is reflected in the small x-ray residuals shown in figure 7.1b that
981 do not reveal a pattern in the relative local offsets across the surface of layer 2. However,
982 figure 7.3 shows that the x-ray and mean cosmics residuals are centered around zero, as is
983 expected for a quadruplet with small relative misalignments between layers.

984 There are three patterns in the residuals on the scatter plot explained by geometry. First,
985 for both datasets the uncertainty in the extrapolated track residuals were larger than the
986 interpolated track residuals because of the extrapolation lever arm. For the x-ray residuals,
987 the effect of the lever arm on the uncertainty was direct since the residual was calculated from
988 a single abstract track; for the mean cosmics residuals it was the widening of the residual
989 distribution due to the extrapolation lever arm that increased the uncertainty in the fitted
990 mean of residuals. Second, residuals calculated through extrapolation tend to be larger
991 because the extrapolation lever arm can produce more extreme values of the track position
992 on the layer of interest. Third, the points in figure 7.2 are geometrically correlated (e.g.
993 they seem to be roughly mirrored around the origin). This is expected since the residuals
994 calculated using a given set of three layers should be geometrically correlated by the local

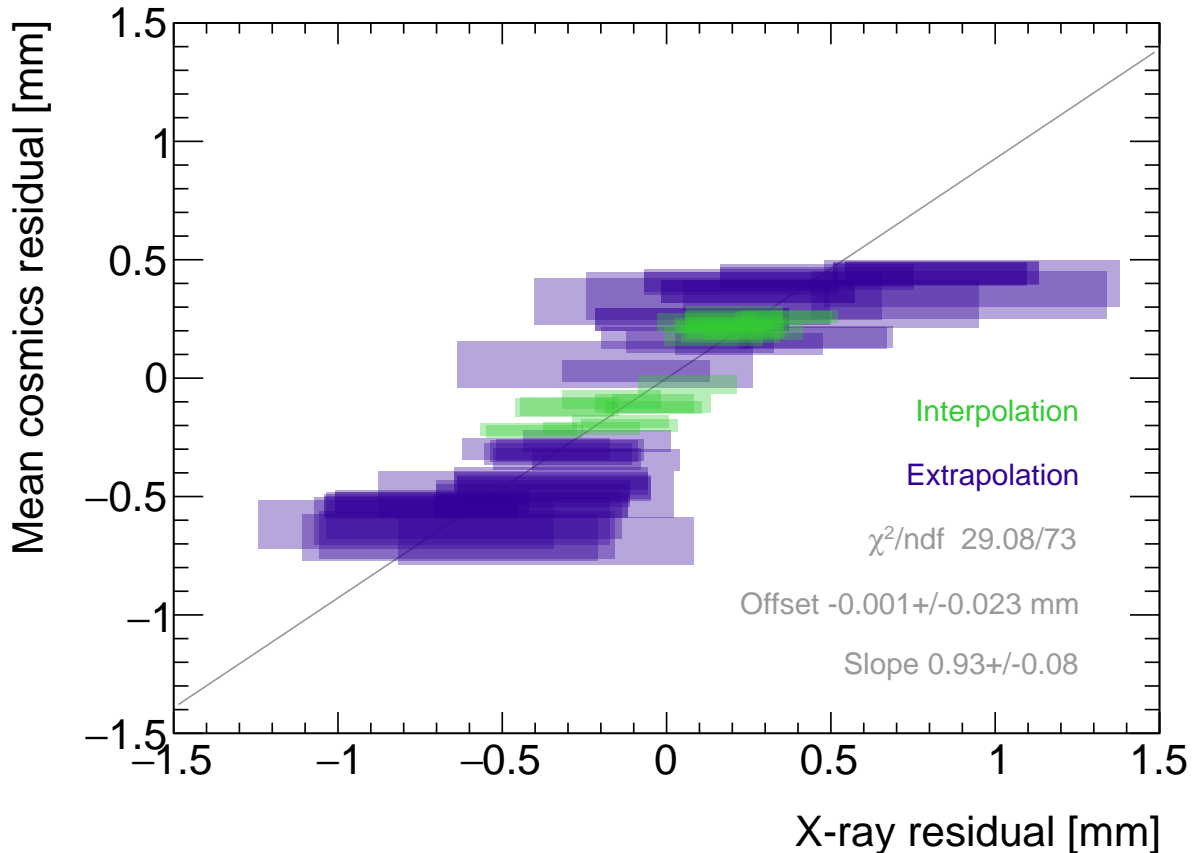


Figure 7.2: Correlation plot between x-ray and mean cosmics residuals for all tracking combinations for QL2.P.11. Each rectangle is centered on an x-ray and mean cosmics residual pair calculated at a given gun position and for a certain tracking combination. The width of the rectangles in x and y are the uncertainty in the x-ray and mean cosmics residual respectively. A printer-friendly version of this plot is available in appendix D.

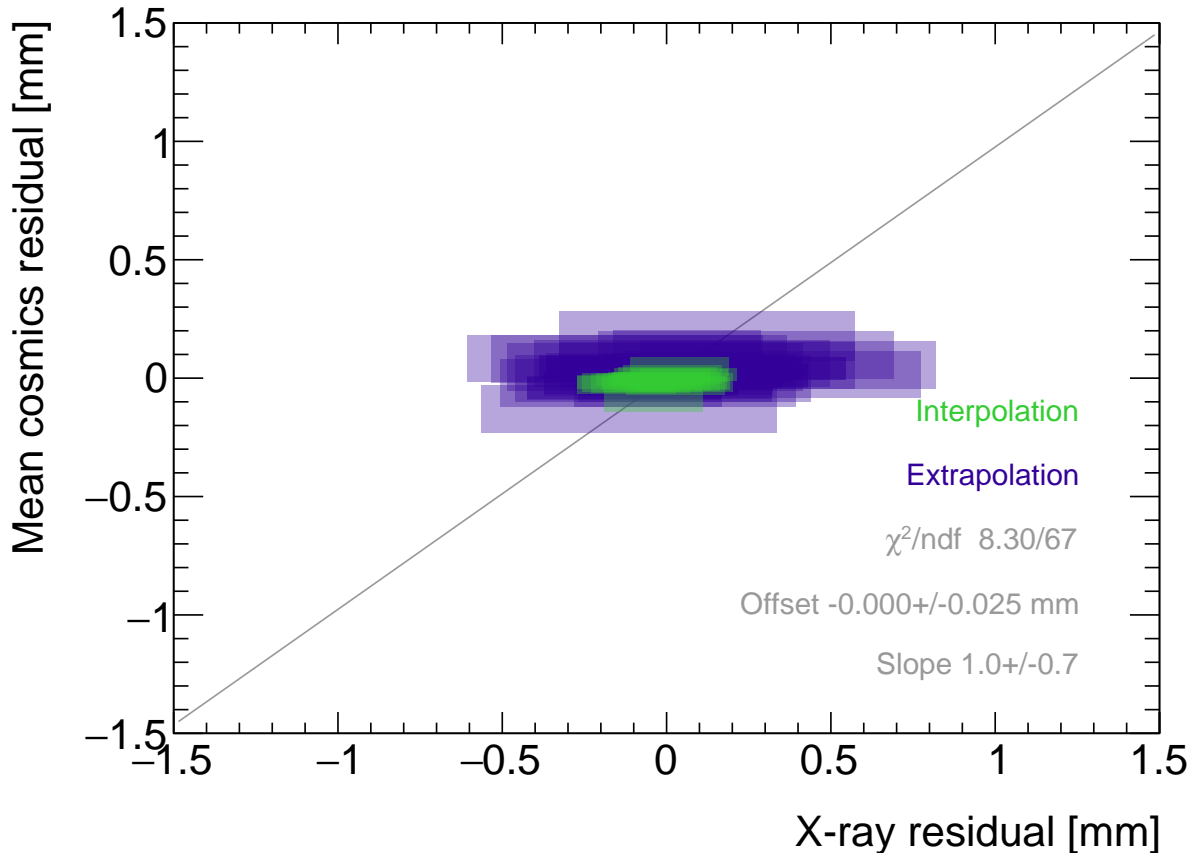


Figure 7.3: Correlation plot between x-ray and mean cosmics residuals for all tracking combinations for quadruplet 2. Each rectangle is centered on an x-ray and mean cosmics residual pair calculated at a given gun position and for a certain tracking combination. The width of the rectangles in x and y are the uncertainty in the x-ray and mean cosmics residual respectively. A printer-friendly version of this plot is available in appendix D.

995 offsets on the fixed layers and the layer of interest (the $d_{local,i}$ on each layer as defined in
996 equation 5.1).

997 7.2 Discussion

998 Several quadruplets were tested for each quadruplet construction geometry built in Canada.
999 Each quadruplet fell into one of the two categories: residuals large enough to see a correlation,
1000 or residuals too small to see a correlation. Since the x-ray and mean cosmics residuals
1001 were measures of the relative local offsets between the layer and the two reference layers,
1002 quadruplets with the largest relative misalignments had the largest range of residuals. the
1003 correlation plots were an easy visual way to identify quadruplets with large relative misalign-
1004 ments.

1005 The most significant limit on measuring the degree of correlation between the x-ray and
1006 mean cosmics residuals was the uncertainty on the x-ray residuals, which stemmed from
1007 the systematic uncertainty of $120\text{ }\mu\text{m}$ in the x-ray beam profile centers used to build the
1008 abstract tracks. For example, in figure 7.3 the uncertainty in the x-ray residuals makes
1009 detecting correlation impossible. The x-ray method was limited primarily by the systematic
1010 uncertainties in the relative alignment of the platforms and the gun, especially the gun angle.

1011 The analysis of certain quadruplets was limited by the availability of data. Sometimes,
1012 less than three layers were surveyed for a given x-ray gun position so no residuals could
1013 be calculated. Too few x-ray residuals prevented the analysis from detecting a significant
1014 correlation, should it even be measurable. Often, the analysis of smaller quadruplets (placed
1015 innermost on the wheel) suffered as a result because they had fewer alignment platforms, and
1016 hence gun positions, on their surfaces. The analysis was also limited to certain quadruplets.
1017 The wedges constructed the earliest (typically small wedges) were surveyed when the x-ray
1018 method was still being designed and so have limited x-ray residuals calculated from beam
1019 profiles of lower quality. In addition, not all cosmic muon test sites had enough front end
1020 electronics to collect data on three layers simultaneously, which is the minimum required to
1021 be able to calculate residuals.

1022 Nonetheless, the comparison of x-ray and cosmics residuals was really to confirm the x-ray
1023 method's ability to measure local offsets with an independent dataset. The x-ray local offsets
1024 allow the calculation of relative local offsets that have been correlated to the cosmics relative
1025 local offsets. Therefore, the analysis of quadruplets with relative local offsets large enough
1026 to detect a correlation validates the x-ray method's ability to measure local offsets.

1027 The potential of using relative local offsets calculated from cosmics data to study relative
1028 alignment between sTGC layers stands on its own. For example, although the x-ray relative

1029 local offsets of QL2.P.8 in figure 7.1b do not reveal a pattern, the variation in the cosmics
1030 relative local offsets do. Identifying the pattern is possible because mean cosmics residuals
1031 can be calculated across the entire area and are sensitive to smaller relative local offsets since
1032 their uncertainty is significantly smaller.

1033 The advantage of the x-ray dataset over the cosmics dataset is that absolute local offsets
1034 are measurable thanks to the reference frame provided by the alignment platforms. This is
1035 required to measure the position of strips in the ATLAS coordinate system to satisfy the
1036 NSWs' precision tracking goals. The x-ray local offsets are being used to build an alignment
1037 model of strips in each quadruplet. It is compelling to imagine using the cosmics relative
1038 local offsets to improve the model considering their precision and ability to capture effects
1039 across the entire area of the quadruplet.

1040 **Chapter 8**

1041 **Outlook and summary**

1042 The cosmic muon dataset was used to independently confirm the absolute local offsets mea-
1043 sured by the x-ray method. The x-ray offsets are being used to complete the sTGC alignment
1044 scheme of the NSWs: the NSW alignment system monitors the position of alignment plat-
1045 forms on the surface of sTGC wedges, and the x-ray measurements provide the offsets of
1046 the strip pattern with respect to each alignment platform. The continuation of this anal-
1047 ysis is detailed next (section 8.1) before summarizing and considering the larger context
1048 (section 8.2).

1049 **8.1 Outlook**

1050 Next all quadruplets with suitable cosmics and x-ray data should be surveyed to flag anom-
1051alous quadruplets (as a first step). If a quadruplet's correlation plot like figure 7.2 or 7.3
1052 reveals an unexpected correlation or has a large scatter, it would indicate an issue with ei-
1053ther the cosmics or x-ray data collection to be investigated further. The uncertainty in each
1054 set of tracking points would inform the interpretation of the anomaly. Then, the quality of
1055 the correlation should be evaluated over all quadruplets instead of individually.
1056 For now, the correlation for the individual quadruplets tested support the use of the x-ray
1057 data to build an alignment model [8]. Work on creating an alignment model is ongoing.
1058 Currently, the algorithm compares the y -position of a local group of strips at each x-ray gun
1059 position as measured by the x-ray and CMM methods in a fit to extract a global slope (m)

1060 and offset (b) per layer, i , where the χ^2 is given by equation 8.1.

$$\chi^2 = \frac{[dy_{cmm,corr} - dy_{xray}]^2}{\delta dy_{xray}^2 + \delta dy_{cmm,corr}^2}, \quad (8.1)$$

1061

$$dy_{cmm,corr} = y_{cmm} + b_i + m_i x - y_{nom} \quad (8.2)$$

1062 Here, dy refers to the corrected CMM and x-ray local offsets, and δdy refers to their re-
1063 spective uncertainties. The CMM measurements were taken before the cathode boards were
1064 assembled into quadruplets, so alignment parameters for the given layer were extracted from
1065 the χ^2 fit by stepping the corrected CMM y -position towards the x-ray y -position by adjust-
1066 ing the layer's slope and offset parameters. The plan is that the alignment parameters will
1067 be provided to the ATLAS experiment's offline software to reconstruct muon tracks from the
1068 NSWs' sTGCs. The large uncertainty on the x-ray local offsets (120 μm) and the sparseness
1069 of the measurements means that including input from other characterization datasets could
1070 reduce the uncertainty on the alignment model parameters.

1071 The uncertainty in the mean cosmics residuals was smaller than the desired position reso-
1072 lution of the sTGCs, so they provide relevant information about strip positions. Moreover,
1073 they can be calculated over the entire area of the quadruplet instead of at specific posi-
1074 tions. It would be great to use the cosmics residuals as input to calculate and reduce the
1075 uncertainty on the alignment parameters. Since mean cosmics residuals can only provide
1076 relative alignment information, one idea would be to use them to constrain the fit of the
1077 alignment parameters. In this case, the alignment parameters would need to be fitted on all
1078 layers at once, and the shifting y -positions on each layer forced to create an abstracted track
1079 residual equal to the local mean cosmics residual (within uncertainty) for each x-ray point.
1080 Or, instead of constraining the fit, it could be penalized if the resulting parameters do not
1081 result in abstracted track residuals equal to the mean cosmics residuals within uncertainty.
1082 Some work on using the three datasets at once in a fit has been started.

1083 8.2 Summary

1084 The LHC [1] will be at the energy frontier of particle physics for at least the next decade,
1085 making it a unique tool with which to study particle physics. With the HL-LHC [2], high
1086 statistics on rare particle physics processes will enable more precise measurements of param-
1087 eters of the Standard Model and increase the sensitivity to signatures of physics beyond the
1088 Standard Model [3]. To capitalize on the increased collision rate, the NSWs of the ATLAS
1089 experiment must be replaced to keep the triggering and tracking performance [5].

1090 Small-strip thin gap chambers are gas ionization chambers optimized for a high rate envi-
1091 ronment [5]. Using the pad electrodes to define a region of interest makes it possible to get
1092 track segments of ~ 1 mrad angular resolution quickly, which will be used as input to check
1093 if a collision originated from the interaction point and should be triggered on or not [5, 53].
1094 sTGCs are also able to provide better than $100 \mu\text{m}$ position resolution on each detector plane
1095 to fulfill precision offline tracking requirements [6].

1096 Ultimately, the positions of the sTGC strip electrodes need to be known in ATLAS to within
1097 $\sim 100 \mu\text{m}$ so that they can deliver the required position resolution. The ATLAS alignment
1098 system will position alignment platforms on the surface of the sTGC wedge, and an alignment
1099 model will be used to position the strips with respect to the alignment platforms [5]. Input
1100 to the alignment model comes from the datasets used to characterize the quadruplets. The
1101 x-ray method [8] is used to measure offsets of strips from their nominal position to achieve
1102 this goal. The alignment model could be built on x-ray data alone, but the sparseness of
1103 and large uncertainty on the local offsets mean that the alignment model could benefit from
1104 more input. Comparing the x-ray offsets to the CMM data [7] allows the effect of inter-layer
1105 misalignments to be isolated and increases the input to the alignment model.

1106 The cosmics dataset was used to confirm the local offsets measured with the x-ray gun. It
1107 provides relative local offsets between sTGC strip layers. The 2D visualizations of relative
1108 local offsets allow personnel to quickly identify areas of misaligned strips and make hypothe-
1109 ses of the physical origin of those misalignments. The correlation seen between the x-ray and
1110 cosmics relative local offsets in quadruplets with large relative misalignments both confirms
1111 the validity of the x-ray local offsets and again is a quick way to identify quadruplets with
1112 large misalignments. Moreover, the mean of track residuals in an area is a robust estimation
1113 of the relative local offset, as shown by the estimation of systematic uncertainties; the relative
1114 local offsets for all two-fixed layer reference frames do not change by more than $100 \mu\text{m}$ given
1115 variation in data collection conditions and analysis algorithms. The cosmics relative local
1116 offsets are therefore relevant input for alignment studies and could improve the alignment
1117 model that will position each strip.

1118 Achieving the required position resolution on each layer of the NSWs in the particle track
1119 bending plane achieves the design momentum resolution for muons ejected towards the end-
1120 caps of ATLAS. Muons are important signatures of electroweak and Higgs sector events
1121 of interest for the ATLAS Collaboration’s future physics goals [5]. Being the second of two
1122 tracking technologies on the NSWs, an effective alignment model of sTGC quadruplets layers
1123 is a necessary part of making the NSWs redundant for 10 or more years of recording collisions
1124 in the High Luminosity era of the LHC.

¹¹²⁵ References

- ¹¹²⁶ [1] L. Evans and P. Bryant. LHC Machine. *Journal of Instrumentation*, 3(S08001), August
¹¹²⁷ 2008.
- ¹¹²⁸ [2] G. Apollinari et al. High-Luminosity Large Hadron Collider (HL-LHC) Technical Design
¹¹²⁹ Report V. 0.1. Technical Report CERN-2017-007-M, CERN, Geneva, September 2017.
- ¹¹³⁰ [3] A. Dainese et al. The physics potential of HL-LHC. In *Input to the European Particle
1131 Physics Strategy Update*, November 2018.
- ¹¹³² [4] The ATLAS Collaboration. The ATLAS Experiment at the CERN Large Hadron Col-
¹¹³³ linder. *Journal of Instrumentation*, 3(08):S08003, August 2008.
- ¹¹³⁴ [5] T. Kawamoto et al. New Small Wheel Technical Design Report. Technical Report
¹¹³⁵ CERN-LHCC-2013-006, ATLAS-TDR-020, CERN, Geneva, June 2013.
- ¹¹³⁶ [6] A. Abusleme et al. Performance of a Full-Size Small-Strip Thin Gap Chamber Prototype
¹¹³⁷ for the ATLAS New Small Wheel Muon Upgrade. *Nuclear Instruments and Methods in
1138 Physics Research Section A: Accelerators, Spectrometers, Detectors and Associated
1139 Equipment*, 817:85–92, May 2016. arXiv: 1509.06329.
- ¹¹⁴⁰ [7] E.M. Carlson. *Results of the 2018 ATLAS sTGC test beam and internal strip alignment
1141 of sTGC detectors*. M.Sc. thesis, University of Victoria, Victoria, Canada, 2019.
- ¹¹⁴² [8] B. Lefebvre. Precision survey of the readout strips of small-strip Thin Gap Chambers
¹¹⁴³ using X-rays for the muon spectrometer upgrade of the ATLAS experiment. *Journal of
1144 Instrumentation*, 15(07):C07013–C07013, July 2020.
- ¹¹⁴⁵ [9] D.J. Griffiths. *Introduction to elementary particles*. Physics textbook. Wiley-VCH,
¹¹⁴⁶ Weinheim, Germany, 2., rev. ed., 5. reprint edition, 2011.
- ¹¹⁴⁷ [10] M.E. Peskin and D.V. Schroeder. *An introduction to quantum field theory*. Addison-
¹¹⁴⁸ Wesley Pub. Co, Reading, Massachusetts, 1995.

- 1149 [11] P.A. Zyla et al. Review of Particle Physics. *PTEP*, 2020(8):083C01, 2020.
- 1150 [12] M. Kobayashi and T. Maskawa. CP-violation in the renormalizable theory of weak
1151 interaction. *Progress of theoretical physics*, 49(2):652–657, February 1973.
- 1152 [13] M.L. Perl et al. Evidence for Anomalous Lepton Production in $\{e\}^{\{+}\backslash\text{ensuremath}{-}\}$
1153 $\{e\}^{\{\backslash\text{ensuremath}{-}\}}\}$ Annihilation. *Physical Review Letters*, 35(22):1489–1492, De-
1154 cember 1975. Publisher: American Physical Society.
- 1155 [14] F. Englert and R. Brout. Broken Symmetry and the Mass of Gauge Vector Mesons.
1156 *Physical Review Letters*, 13(9):321–323, August 1964. Publisher: American Physical
1157 Society.
- 1158 [15] P.W. Higgs. Broken symmetries, massless particles and gauge fields. *Physics Letters*,
1159 12(2):132–133, September 1964.
- 1160 [16] D. Galbraith and C. Burgard. UX: Standard Model of the Stan-
1161 dard Model, November 2013. [http://davidgalbraith.org/portfolio/
1162 ux-standard-model-of-the-standard-model/](http://davidgalbraith.org/portfolio/ux-standard-model-of-the-standard-model/) last accessed on 2021-09-30.
- 1163 [17] C.A. Bertulani. *Nuclear physics in a nutshell*. In a nutshell. Princeton University Press,
1164 Princeton, N.J, 2007. OCLC: ocm85690422.
- 1165 [18] B.W. Carroll and D.A. Ostlie. *An introduction to modern astrophysics*. Pearson
1166 Addison-Wesley, San Francisco, 2nd ed edition, 2007. OCLC: ocm69020924.
- 1167 [19] M. Boezio and E. Mocchiutti. Chemical composition of galactic cosmic rays with space
1168 experiments. *Astroparticle Physics*, 39-40:95–108, December 2012.
- 1169 [20] The SNO Collaboration. Combined analysis of all three phases of solar neutrino data
1170 from the sudbury neutrino observatory. *Phys. Rev. C*, 88:025501, August 2013.
- 1171 [21] B. Pontecorvo. Neutrino Experiments and the Problem of Conservation of Leptonic
1172 Charge. *Soviet Physics—JETP*, 53:1717–1725, 1967.
- 1173 [22] S.M. Bilenky and S.T. Petcov. Massive neutrinos and neutrino oscillations. *Reviews of
1174 Modern Physics*, 59(3):671–754, July 1987.
- 1175 [23] B. Young. A survey of dark matter and related topics in cosmology. *Frontiers of Physics*,
1176 12(2):121201, April 2017.
- 1177 [24] C. Muñoz. Dark matter detection in the light of recent experimental results. *International
1178 Journal of Modern Physics A*, 19(19):3093–3169, July 2004.

- 1179 [25] G. Arnison et al. Experimental observation of isolated large transverse energy elec-
1180 trons with associated missing energy at s=540 GeV. *Physics Letters B*, 122(1):103–116,
1181 February 1983.
- 1182 [26] M. Banner et al. Observation of single isolated electrons of high transverse momentum
1183 in events with missing transverse energy at the CERN pp collider. *Physics Letters B*,
1184 122(5):476–485, March 1983.
- 1185 [27] G. Arnison et al. Experimental observation of lepton pairs of invariant mass around 95
1186 GeV/c² at the CERN SPS collider. *Physics Letters B*, 126(5):398–410, July 1983.
- 1187 [28] P. Bagnaia et al. Evidence for Z → e⁺e⁻ at the CERN pp collider. *Physics Letters B*,
1188 129(1):130–140, 1983.
- 1189 [29] The CDF Collaboration. Observation of Top Quark Production in $\bar{p}p$ Collisions with
1190 the Collider Detector at Fermilab. *Physical Review Letters*, 74(14):2626–2631, April
1191 1995. Publisher: American Physical Society.
- 1192 [30] The D0 Collaboration. Observation of the Top Quark. *Physical Review Letters*,
1193 74(14):2632–2637, April 1995. Publisher: American Physical Society.
- 1194 [31] The ATLAS Collaboration. Observation of a new particle in the search for the Standard
1195 Model Higgs boson with the ATLAS detector at the LHC. *Physics Letters B*, 716(1):1–
1196 29, September 2012. arXiv: 1207.7214.
- 1197 [32] The CMS Collaboration. Observation of a new boson at a mass of 125 GeV with the
1198 CMS experiment at the LHC. *Physics Letters B*, 716(1):30–61, September 2012. arXiv:
1199 1207.7235.
- 1200 [33] Standard Model Summary Plots June 2021, June 2021. <https://atlas.web.cern.ch/Atlas/GROUPS/PHYSICS/PUBNOTES/ATL-PHYS-PUB-2021-032/> last accessed on 2021-
1201 09-30.
- 1203 [34] O.S. Brüning et al. *LHC Design Report*. CERN Yellow Reports: Monographs. Geneva,
1204 2004.
- 1205 [35] ATLAS luminosity public results run-1, March 2011. <https://twiki.cern.ch/twiki/bin/view/AtlasPublic/LuminosityPublicResults> last accessed on 2021-09-20.
- 1207 [36] ATLAS luminosity public results run-2, July 2015. <https://twiki.cern.ch/twiki/bin/view/AtlasPublic/LuminosityPublicResultsRun2> last accessed on 2021-09-20.

- 1209 [37] The European Strategy for Particle Physics. Technical Report CERN/2685, CERN,
1210 2006. Adopted by the CERN council at a special session at ministerial level in Lisbon
1211 in 2006.
- 1212 [38] HiLumi HL-LHC Project. LHC/HL-LHC plan (last update january 2021). <https://hilumilhc.web.cern.ch/content/hl-lhc-project>, last accessed on 2021-09-09.
- 1214 [39] M. Cepeda et al. Report from Working Group 2: Higgs Physics at the HL-LHC and
1215 HE-LHC. *CERN Yellow Reports Monographs*, 7:221–584. 364 p, Dec 2018.
- 1216 [40] ATLAS inner detector : Technical Design Report, 1. Technical Report CERN-LHCC-
1217 97-016, CERN, April 1997. ISBN: 9789290831020 Publication Title: CERN Document
1218 Server.
- 1219 [41] S. Haywood, L. Rossi, R. Nickerson, and A. Romanouk. ATLAS inner detector :
1220 Technical Design Report, 2. Technical Report CERN-LHCC-97-017, CERN, April 1997.
1221 ISBN: 9789290831037 Publication Title: CERN Document Server.
- 1222 [42] C. Grupen, B.A. Shwartz, and H. Spieler. *Particle detectors*. Cambridge University
1223 Press, Cambridge, UK; New York, 2008. OCLC: 1105536566.
- 1224 [43] ATLAS liquid-argon calorimeter : Technical Design Report. Technical Report CERN-
1225 LHCC-96-041, CERN, 1996. ISBN: 9789290830900 Publication Title: CERN Document
1226 Server.
- 1227 [44] ATLAS tile calorimeter : Technical Design Report. Technical Report CERN-LHCC-96-
1228 042, CERN, 1996. ISBN: 9789290830917 Publication Title: CERN Document Server.
- 1229 [45] The ATLAS Collaboration. ATLAS Muon Spectrometer: Technical Design Report.
1230 Technical Report CERN-LHCC-97-022, CERN, Geneva, 1997.
- 1231 [46] ATLAS magnet system : Technical Design Report, 1. Technical Report CERN-LHCC-
1232 97-018, CERN, April 1997. ISBN: 9789290831044 Publication Title: CERN Document
1233 Server.
- 1234 [47] The ATLAS Collaboration. Performance of the ATLAS muon trigger in pp collisions
1235 at $\sqrt{s} = 8$ TeV. *The European Physical Journal C*, 75(3):120, March 2015. arXiv:
1236 1408.3179.
- 1237 [48] S. Aefsky et al. The Optical Alignment System of the ATLAS Muon Spectrometer End-
1238 caps. *Journal of Instrumentation*, 3(11):P11005–P11005, November 2008. Publisher:
1239 IOP Publishing.

- 1240 [49] ATLAS level-1 trigger : Technical Design Report. Technical Report CERN-LHCC-98-
1241 014, CERN, August 1998. ISBN: 9789290831280 Publication Title: CERN Document
1242 Server.
- 1243 [50] A. Ruiz Martínez. The run-2 ATLAS trigger system. *Journal of Physics: Conference
1244 Series*, 762:012003, October 2016.
- 1245 [51] Technical Design Report for the Phase-II Upgrade of the ATLAS TDAQ System. Tech-
1246 nical Report CERN-LHCC-2017-020, ATLAS-TDR-029, CERN, Geneva, September
1247 2017.
- 1248 [52] P. Jenni, M. Nessi, M. Nordberg, and K. Smith. ATLAS high-level trigger, data-
1249 acquisition and controls : Technical Design Report. Technical Report CERN-LHCC-
1250 2003-022, CERN, July 2003.
- 1251 [53] E. Perez Codina. Small-strip Thin Gap Chambers for the muon spectrometer upgrade of
1252 the ATLAS experiment. *Nuclear Instruments and Methods in Physics Research Section
1253 A: Accelerators, Spectrometers, Detectors and Associated Equipment*, 824:559–561, July
1254 2016.
- 1255 [54] J. Townsend. *Electricity in gases*. Clarendon Press, Oxford, 1915.
- 1256 [55] S. Majewski, G. Charpak, A. Breskin, and G. Mikenberg. A thin multiwire chamber
1257 operating in the high multiplication mode. *Nuclear Instruments and Methods*, 217:265–
1258 271, 1983.
- 1259 [56] E. Gatti, A. Longoni, H. Okuno, and P. Semenza. Optimum geometry for strip cathodes
1260 or grids in MWPC for avalanche localization along the anode wires. *Nuclear Instruments
1261 and Methods*, 163(1):83–92, July 1979.
- 1262 [57] G. Battistoni et al. Resistive cathode transparency. *Nuclear Instruments and Methods
1263 in Physics Research*, 202(3):459–464, November 1982.
- 1264 [58] B. Lefebvre. *Characterization studies of small-strip Thin Gap Chambers for the ATLAS
1265 Upgrade*. PhD thesis, McGill University, Montreal, Canada, 2018.
- 1266 [59] P.K.F. Grieder. *Cosmic rays at Earth: researcher’s reference manual and data book*.
1267 Elsevier Science Ltd, Amsterdam, 1st ed edition, 2001.
- 1268 [60] R. Keyes et al. Development and characterization of a gas system and its associated
1269 slow-control system for an ATLAS small-strip thin gap chamber testing facility. *Journal
1270 of Instrumentation*, 12(04):P04027–P04027, April 2017.

- 1271 [61] Georgios Iakovidis. VMM3, an ASIC for Micropattern Detectors. Technical Report
1272 ATL-MUON-PROC-2018-003, CERN, Geneva, March 2018.
- 1273 [62] B. Chen. *Calibration Studies of the Front-End Electronics for the ATLAS New Small*
1274 *Wheel Project*. M.Sc. thesis, McGill University, Montreal, Canada, 2019.
- 1275 [63] R. Brun and F. Rademakers. ROOT: An object oriented data analysis framework. *Nu-*
1276 *clear Instruments and Methods in Physics Research Section A: Accelerators, Spectrome-*
1277 *ters, Detectors and Associated Equipment*, 389:81–86, 1997. See also ”ROOT” [software],
1278 Release 6.18/02, 23/08/2019, (<https://zenodo.org/record/3895860#.YVJW6n0pCHs>).
- 1279 [64] F. Sauli. Principles of operation of multiwire proportional and drift chambers. In *Cern*
1280 *Yellow Reports: Monographs*, page 92 p, Geneva, 1977. CERN, CERN. CERN, Geneva,
1281 1975 - 1976.
- 1282 [65] M. Hatlo et al. Developments of mathematical software libraries for the LHC experi-
1283 ments. *IEEE Transactions on Nuclear Science*, 52:2818–2822, 2005.
- 1284 [66] H. Guo. A Simple Algorithm for Fitting a Gaussian Function [DSP Tips and Tricks].
1285 *IEEE Signal Processing Magazine*, 28(5):134–137, September 2011.
- 1286 [67] B. Stelzer. The New Small Wheel Upgrade Project of the ATLAS Experiment. *Nuclear*
1287 *and Particle Physics Proceedings*, 273-275:1160–1165, April 2016.
- 1288 [68] X. Zhao et al. Cosmic test of sTGC detector prototype made in China for ATLAS
1289 experiment upgrade. *Nuclear Instruments and Methods in Physics Research Section A:*
1290 *Accelerators, Spectrometers, Detectors and Associated Equipment*, 927:257–261, May
1291 2019.

¹²⁹² APPENDICES

1293 **Appendix A**

1294 **Uncertainty in cluster positions**

1295 **A.1 Cluster definition**

1296 A cluster is a series of contiguous strip channels on a layer with non-zero amplitude, all
1297 part of the same trigger and having the same event number [58]. Clusters result from the
1298 drift of ionization products generate in the ionization avalanche caused by a muon [54]. The
1299 peak-detector-output (PDO) of the signal on each strip of a cluster is fit with a Gaussian.
1300 The y-position of a particle as it passed through the layer is mean of the cluster, referred to
1301 here as the hit position.

1302 **A.2 Effect of fit algorithm on cluster mean**

1303 The clusters were fit with Guo's method [66] and Minuit2 for ROOT [65]. The difference in
1304 cluster means between the two algorithms is shown in figure A.1.

1305 The RMS of the distribution in figure A.1 is $57 \mu\text{m}$, which is much larger than the statistical
1306 uncertainty in the mean for the Minuit2 algorithm, which peaks around $7 \mu\text{m}$. An RMS of
1307 $60 \mu\text{m}$ is common for data taken with most quadruplets at 3.1 kV. Therefore, the uncertainty
1308 in the y-hit positions is assigned $60 \mu\text{m}$.

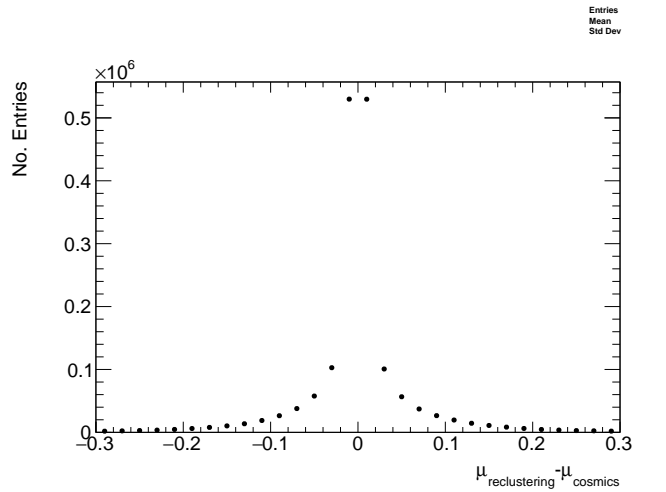


Figure A.1: The difference between cluster means calculated with Guo's method [66] in `tgc_analysis/CosmicsAnalysis` and Minuit2 for ROOT [65] in `strip_position_analysis/ReClustering` for data collected with QL2.P.8 at 3.1 kV.

1309 **A.3 Effect of uncertainty in cluster mean on track residuals**

1310

1311 The uncertainty assigned to the hit position affected the uncertainty in the extrapolated/interpolated
1312 position of the track, and in the residuals. The bin size of the residual distributions was set
1313 to 200 μm because that was the uncertainty in the residuals calculated from the tracks with
1314 the least favourable geometry (like tracks built from hits on layers 1 and 2 and extrapolated
1315 to layer 4).

₁₃₁₆ **Appendix B**

₁₃₁₇ **Study of cosmics for alignment
analysis statistical uncertainty**

₁₃₁₉ Typically, one million triggers (cosmic muon events, noise, photons and δ -rays) were collected
₁₃₂₀ for each Canadian quadruplet at McGill University, resulting in roughly half the number of
₁₃₂₁ viable tracks after cuts. For QS3.P.18, 3.5 million triggers were collected. To gauge the
₁₃₂₂ sensitivity of the analysis to the available statistics, partitions of this data with each with
₁₃₂₃ a different number of triggers were analyzed separately. Ultimately, the quantity of interest
₁₃₂₄ was the gaussian mean of the residual distribution in regions of interest, so the peak in the
₁₃₂₅ distribution of the statistical uncertainty in the residual means for each area of interest for
₁₃₂₆ a specific tracking combination was used to gauge the quality of the analysis. How the peak
₁₃₂₇ in the residual mean uncertainty distribution changes with the number of triggers is shown
₁₃₂₈ in figure for tracks on layer 1 built from layers 3 and 4 [B.1](#).

₁₃₂₉ The uncertainty is already around 20 μm at 1 million triggers, suitable for distinguishing
₁₃₃₀ differences in offsets of order 50 μm as required. Although increased statistics could decrease
₁₃₃₁ the statistical uncertainty, it is not required for the goals of this analysis. Moreoever, the
₁₃₃₂ systematic uncertainty is around 50 μm and the systematic uncertainty on the x-ray residuals
₁₃₃₃ is 150 μm so the statistical uncertainty of 20 μm is nearly negligible.

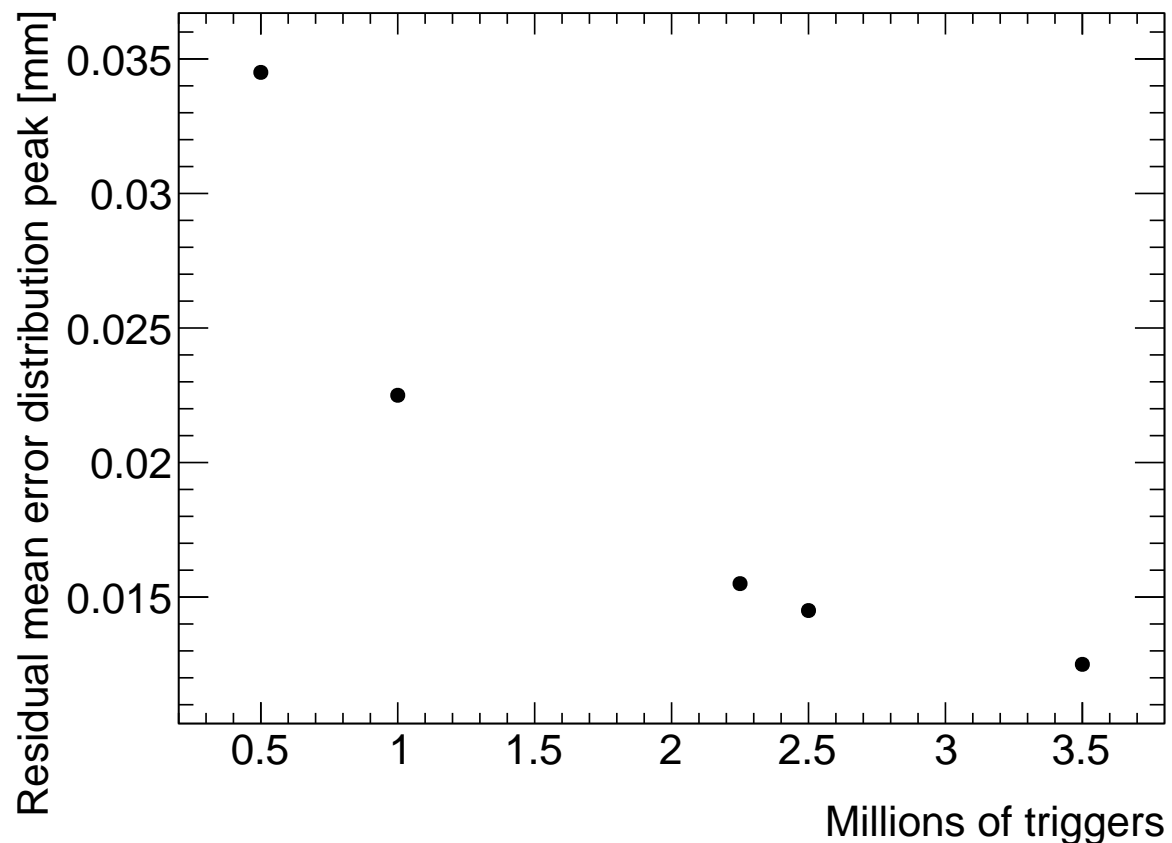


Figure B.1: How the peak of the distributions of uncertainties in the residual means in regions of interest for tracks on layer 1 built from layers 3 and 4 changed with the number of triggers used in the analysis. The distribution falls off as $\frac{1}{\sqrt{N}}$ as expected.

¹³³⁴ Appendix C

¹³³⁵ Study of systematic uncertainties ¹³³⁶ when using cosmics data for ¹³³⁷ alignment studies

¹³³⁸ C.1 Residual distribution fit function

¹³³⁹ The distribution of residuals should be modelled by a double gaussian fit[58]:

$$G(r) = A_s \exp \left[\frac{-(r - \mu)^2}{2\sigma_s^2} \right] + A_b \exp \left[\frac{-(r - \mu)^2}{2\sigma_b^2} \right] \quad (\text{C.1})$$

¹³⁴⁰ where r is the residual, A is the gaussian amplitude, μ is the gaussian mean, σ is the
¹³⁴¹ gaussian sigma, and the subscripts s and b stand for signal and background respectively.
¹³⁴² One gaussian captures the real (signal) tracks and the other captures the tracks built from
¹³⁴³ noise (background). The gaussian with the smaller width is identified as the signal.

¹³⁴⁴ A single gaussian fit failed less often than a double gaussian fit. The gaussian fits were
¹³⁴⁵ performed by initially estimating the amplitude to be 100 tracks, the gaussian mean to be
¹³⁴⁶ the histogram mean, and gaussian σ to be the RMS. The fit range was restricted to ± 1 RMS
¹³⁴⁷ from the histogram mean. The modification helped the gaussian fit capture the signal peak.
¹³⁴⁸ An example residual distribution is shown in figure C.1.

¹³⁴⁹ For all residual distributions in 100 mm by 100 mm bins on layer 4 built from hits on layers 1
¹³⁵⁰ and 2, the difference in gaussian and double gaussian means and σ 's is shown in figure C.2.
¹³⁵¹ Since the RMS of the residual mean differences distribution is less than 50 μm the gaussian

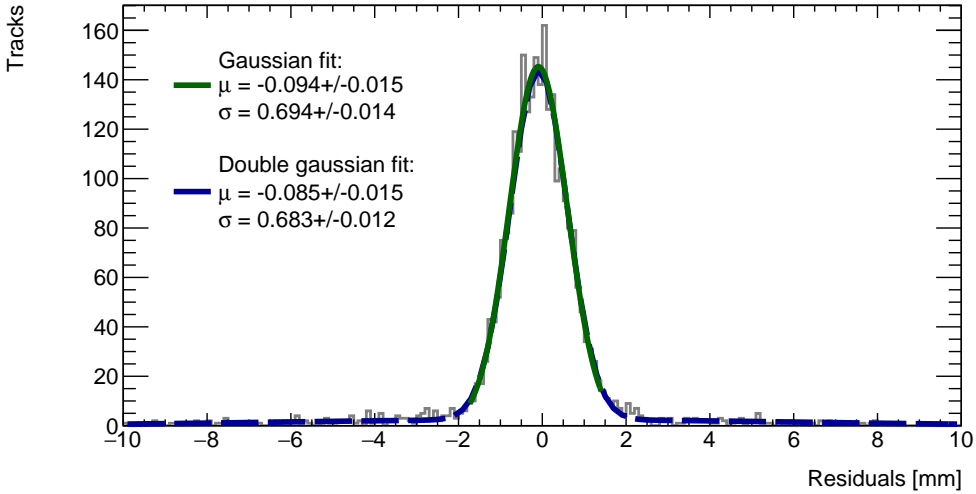


Figure C.1: Residual distribution for tracks on layer 4 built from hits on layers 1 and 2 for $x \in [-3.00, 97.00]$, $y \in [394.60, 494.60]$ mm for QL2.P.8 fit with a double gaussian and a single gaussian in a range of ± 1 RMS from the histogram mean.

1352 fit gave the same result within the required precision. Moreover, this is for the tracking
1353 combination with the worst extrapolation lever arm and the widest distribution of mean
1354 differences; the interpolation combinations have narrower distributions.

1355 The gaussian σ should be larger than the double gaussian σ because the gaussian distribution
1356 includes the effect of the noise tracks with large residuals, while the double gaussian models
1357 signal and background residuals separately. For this analysis, only the residual mean was
1358 important, so the systematic overestimate of the signal σ in the gaussian fit shown on the
1359 right of figure C.2 was allowed.

1360 C.2 Cosmic muon data collection voltage

1361 Cosmic muon data was collected at 2.9 kV and 3.1 kV because although 2.9 kV is closer to
1362 the operating conditions the chambers will be subject to in ATLAS, the extra gain provided
1363 by operating at 3.1 kV increased the signal to noise ratio for pad signals. Also, the tracking
1364 efficiency was higher with data collected at 3.1 kV. The difference in gain affected the relative
1365 population of clusters of different sizes, which in turn affected the uncertainty in the strip hit
1366 positions on each layer, the uncertainty in the track positions and the residual distributions.
1367 The residual distributions for 3.1 kV data are narrower, as shown in figure C.3.

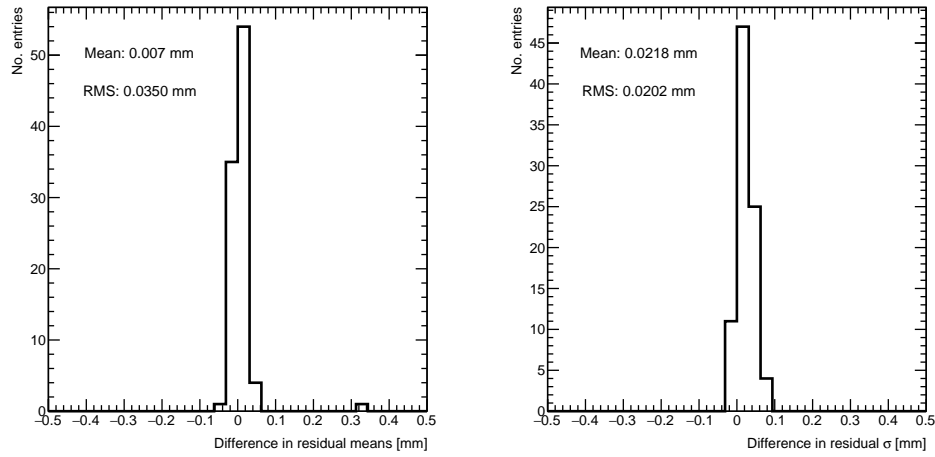


Figure C.2: Difference in residual distribution means and σ 's for a gaussian and double gaussian fit, for all residual distributions in 100 mm by 100 mm bins on layer 4 built from hits on layers 1 and 2 for QL2.P.8.

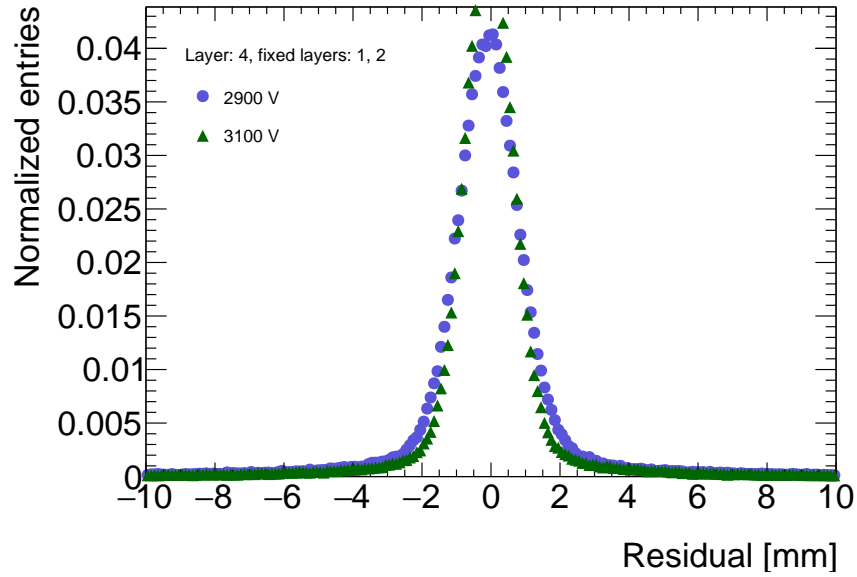
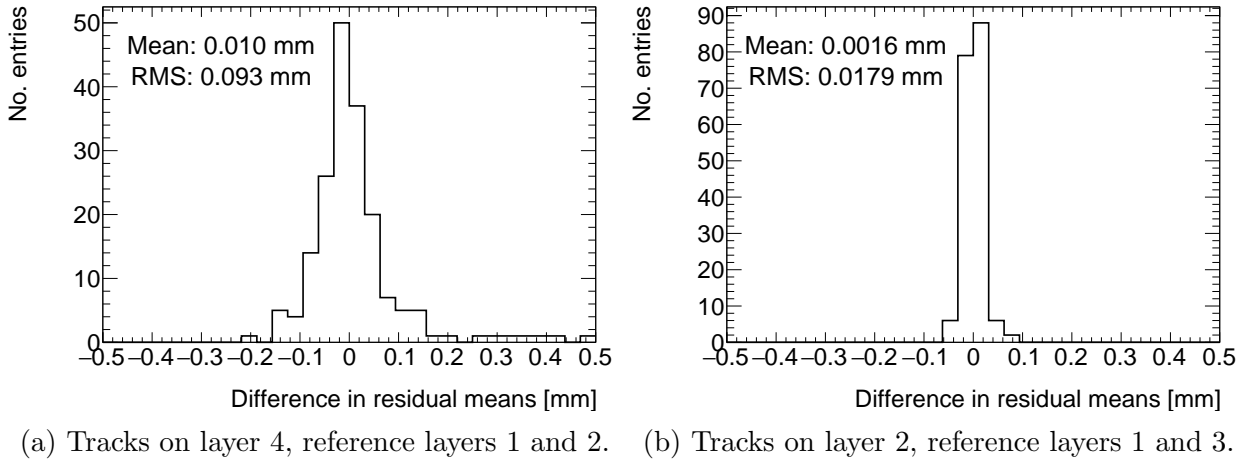


Figure C.3: Residual distribution for tracks on layer 4 built from hits on layers 1 and 2 for QL2.P.8 for data collected at 2.9 kV and 3.1 kV.



(a) Tracks on layer 4, reference layers 1 and 2. (b) Tracks on layer 2, reference layers 1 and 3.

Figure C.4: Difference in residual means for data collected with QL2.P.8 at 2.9 kV and 3.1 kV respectively in 100 mm by 100 mm bins for (a) tracks on layer 4 built from hits on layers 1 and 2 and (b) tracks on layer 2 built from hits on layers 1 and 3.

1368 Neither dataset is better for calculating the mean of residuals in a given area, so a systematic
 1369 uncertainty can be assigned based on the difference in residual means calculated for 2.9 kV
 1370 and 3.1 kV data; namely, the systematic uncertainty was approximated as the RMS of the
 1371 residual mean difference distribution. Data taken with QL2.P.8 was used to estimate the
 1372 RMS, as in figure C.4a.

1373 Tracks built from hits on layers 1 and 2 and extrapolated to layer 4 have the worst lever arm
 1374 and hence the most uncertainty. The width of the distribution for geometrically favourable
 1375 tracks are much narrower. The narrowest width of the residual mean difference distribution
 1376 is for tracks on layer 2 built from hits on layers 1 and 3 (see figure C.4b).

1377 Therefore, for each tracking combination, a systematic uncertainty equal to the RMS of the
 1378 residual mean difference distribution was assigned.

1379 C.3 Cluster fit algorithm

1380 To ensure that changing the cluster fitting algorithm like in appendix A would not change
 1381 the calculated mean of residuals in each region of interest significantly, the residual means
 1382 were compared in both cases. The distribution of the difference in residual means is plotted
 1383 in figure C.5 for the tracking combination with the worst extrapolation lever arm.

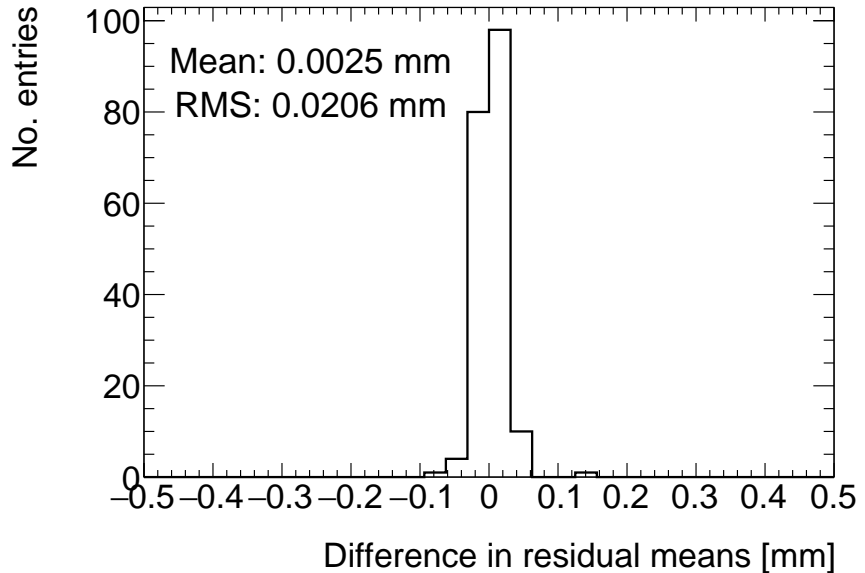


Figure C.5: Difference in residual means when the cluster fit algorithm is `Minuit2` [65] versus Guo’s method [66] for tracks on layer 4 built from hits on layers 1 and 2 for QL2.P.8.

1384 The other tracking combinations had smaller RMS values. Differences on the order of 50 μm
 1385 are important, so figure C.5 shows that the clustering algorithm had a small but notable
 1386 effect. Therefore, the RMS for each tracking combination will be used to add a systematic
 1387 uncertainty on the residual means.

1388 C.4 Differential non-linearity

1389 Definition

1390 In this context, differential non-linearity (DNL) is when the reconstructed cluster mean is
 1391 biased by the fit of the discretely sampled PDO distribution over the strips. The bias depends
 1392 on the relative position of the avalanche with respect to the center of the closest strip. For a
 1393 summary of DNL, refer to page 40 of Lefebvre’s thesis [58] and for an example application,
 1394 refer to [6].

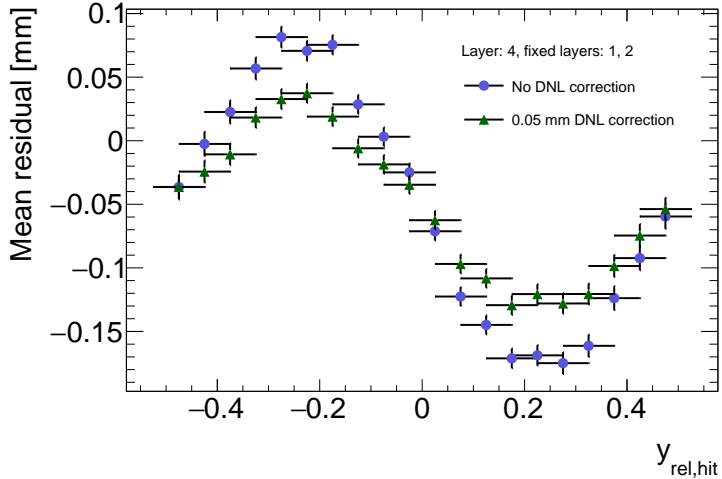


Figure C.6: Effect applying a 50 μm DNL correction to the cluster means on the residual vs y_{rel} distribution for tracks built from layers 1 and 2 and extrapolated to layer 4 for QL2.P.8.

1395 **Application and effect of DNL**

1396 The cluster mean was corrected for DNL using the equation:

$$y' = y + a \sin(2\pi y_{rel}) \quad (\text{C.2})$$

1397 where y is the cluster mean, y_{rel} is the relative position of the cluster mean with respect to
1398 the strip's center, a is the amplitude of the correction, and y' is the corrected cluster mean.
1399 The amplitude can be derived by comparing the reconstructed hit position to the expected
1400 hit position, as done in Abusleme, 2016 [6]. With cosmic muons, there is no reference hit
1401 position to compare to, so track residuals were used as a proxy [58]. The hallmark of the DNL
1402 effect is the periodic pattern in the residual versus y_{rel} profile, and the effect of correcting
1403 the cluster means using an amplitude of 50 μm is shown in figure C.6. An amplitude of
1404 50 μm was based on Lefebvre's estimate of the DNL amplitudes by layer, quadruplet and
1405 cluster size using exclusive cosmic muon tracks in `tgc_analysis/CosmicsAnalysis`. Little
1406 variation was seen in the amplitude parameters with respect to the quadruplet tested, the
1407 layer and the cluster size so a universal correction was used.

1408 Although the correction is not large enough in this case, the figure shows that the correction
1409 does reduce the DNL effect. Slightly better performance is seen in the interpolation tracking
1410 combinations where the quality of the residuals is better. DNL corrections for cosmic muon
1411 data are difficult because the DNL effect is obscured by the effect of misalignments and

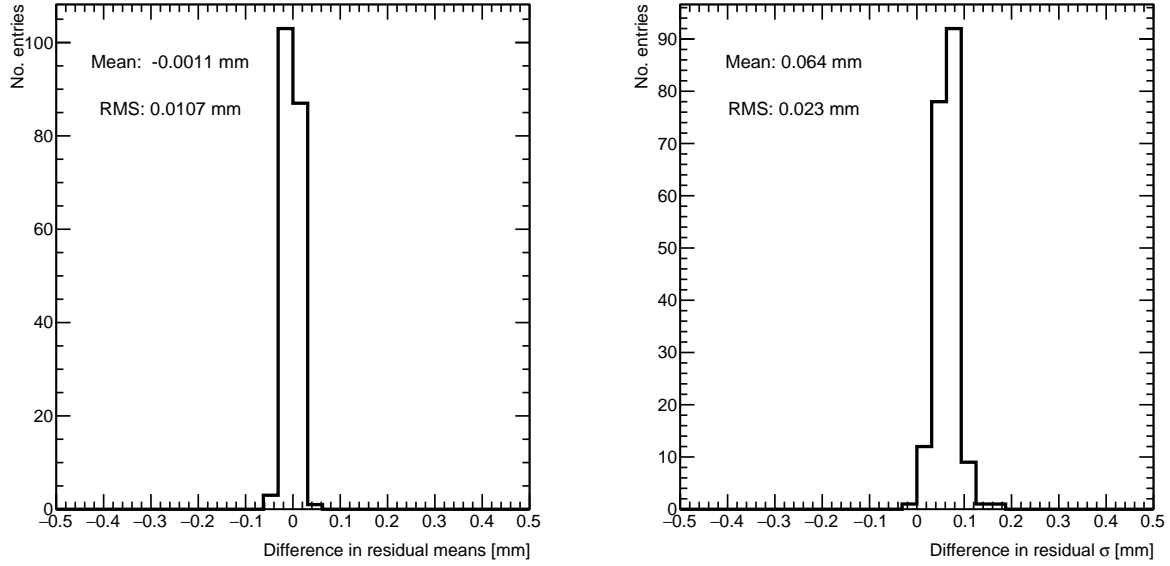


Figure C.7: Difference in residual distribution means and σ 's with and without DNL correction for residuals on layer 4 from reference layers 1 and 2 for QL2.P.8.

1412 noise. Misalignments cause the center of the sine pattern in figure C.6 to be shifted off of
 1413 zero, since the mean of residuals is shifted.

1414 In figure C.7, it is apparent that the effect of the DNL correction on the mean of the
 1415 residual distribution in 100 mm by 100 mm areas is on the order of micrometers in the worst
 1416 extrapolation case. Although the σ 's of the residual distributions shrink with the DNL
 1417 correction, the mean is the parameter of interest. Therefore, for this analysis DNL was not
 1418 corrected for.

1419 The σ 's of the residual distributions do shrink with the DNL correction but not so much to
 1420 affect the residual means, which are the important parameter for this analysis. Therefore,
 1421 since the effect of the DNL correction is negligible, it was not pursued further.

₁₄₂₂ Appendix D

₁₄₂₃ Printable plots

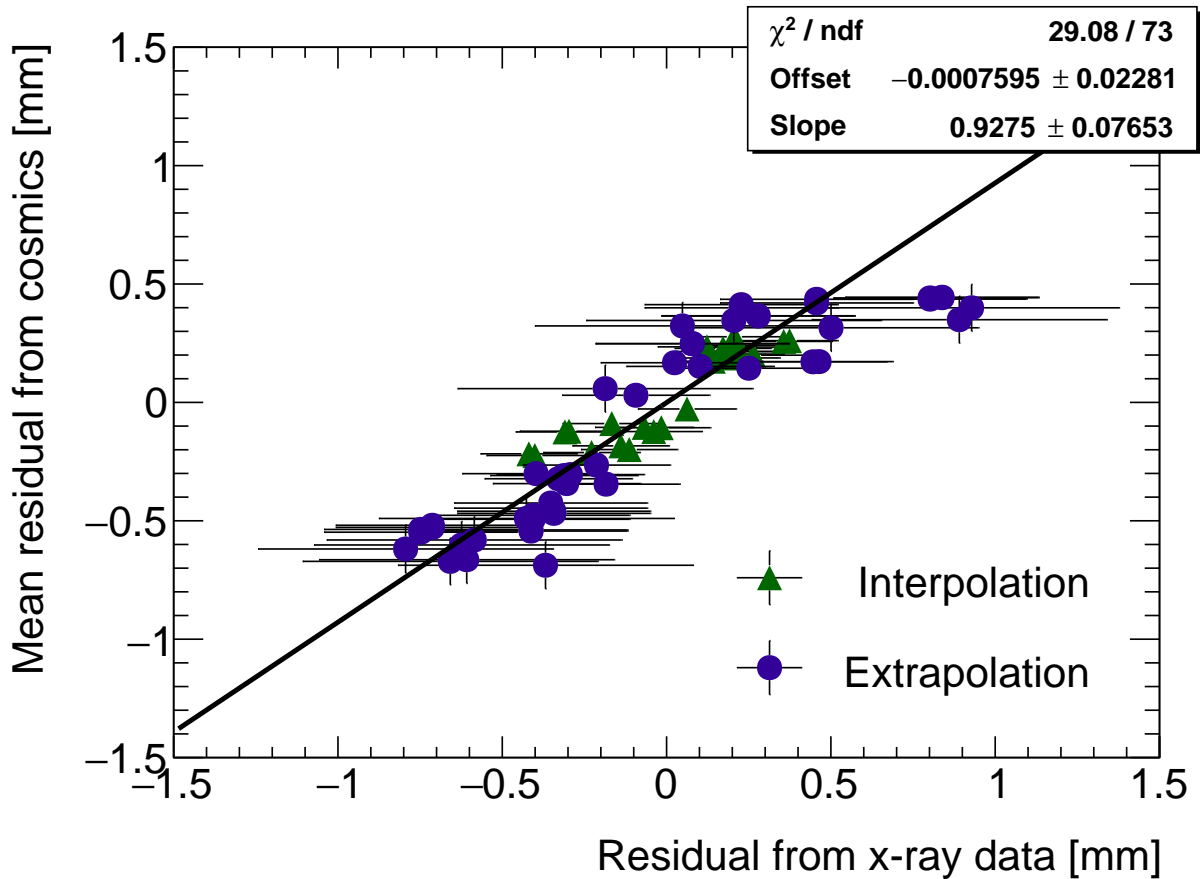


Figure D.1: Correlation plot between x-ray and cosmics residuals for all tracking combinations for QL2.P.11. Each rectangle is centered on an x-ray and mean cosmics residual pair. The width of the rectangles in x and y are the uncertainty in the x-ray and mean cosmics residual respectively. This is a printable version of figure 7.2 in section 7.1.

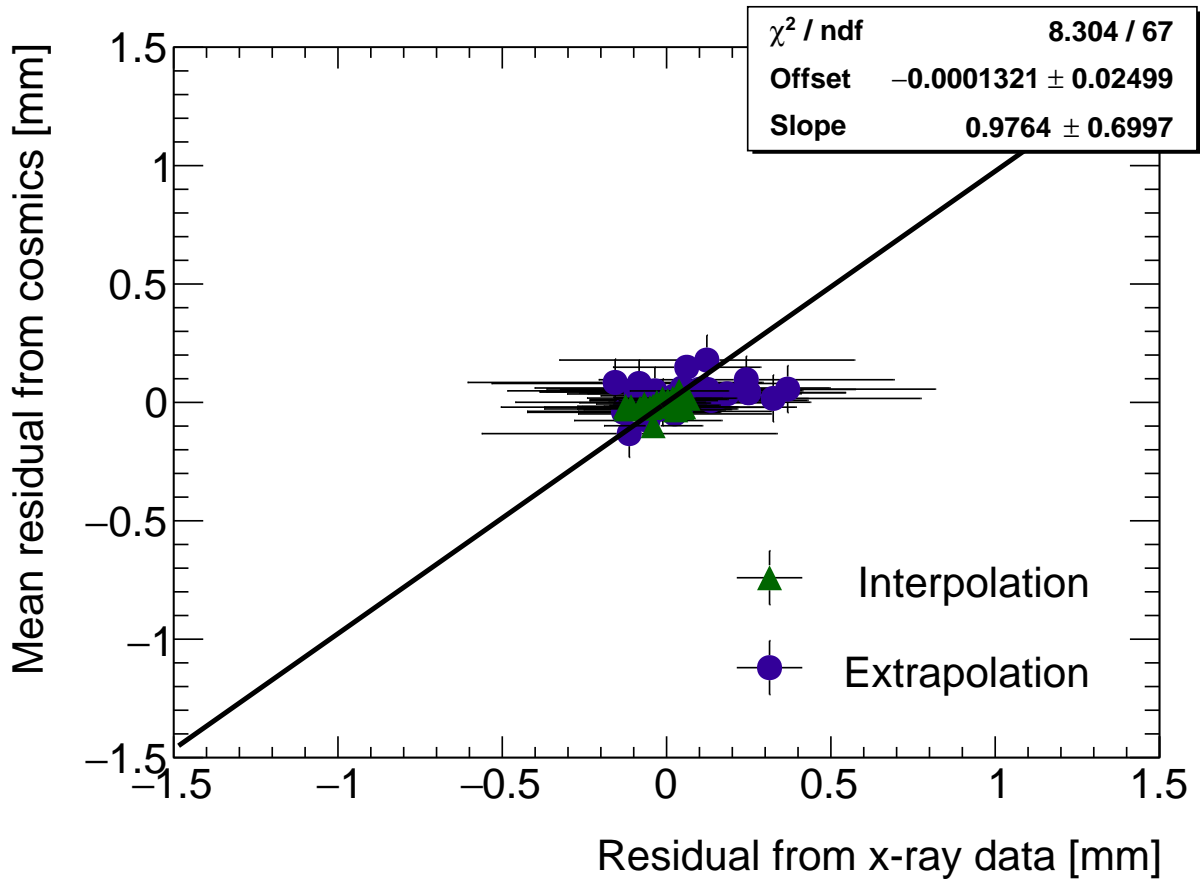


Figure D.2: Correlation plot between x-ray and cosmics residuals for all tracking combinations for QL2.P.8. Each rectangle is centered on an x-ray and mean cosmics residual pair. The width of the rectangles in x and y are the uncertainty in the x-ray and mean cosmics residual respectively. This is a printable version of figure 7.3 in section 7.1.